UNIVERSITY OF NOVA GORICA
GRADUATE SCHOOL

CONDUCTIVE ATOMIC FORCE MICROSCOPY OF QUANTUM DOTS AND QUANTUM RINGS

MASTER'S THESIS

Tomaž Mlakar

Mentor: dr. Stefan Heun

Nova Gorica, 2011

Abstract

The properties of self-assembled InAs/GaAs quantum dots and rings are investigated by conductive atomic force microscopy (C-AFM). Two-dimensional C-AFM current maps and local current-voltage curves measured on quantum rings show a lower conductivity of the central ring hole as compared to rim and surrounding planar region in the whole tip bias range investigated. This result is quite surprising since various experimental results published agree on the fact that the central hole is the region with the highest relative In concentration. Numerical simulations of as-grown samples show that the difference in conductivities between the central hole and the rim depends on the tip bias, which is clearly incompatible with experimental results. However, it needs to be considered that the samples were exposed to air which causes the topmost layers to oxidize. Including the presence of a surface oxide into numerical simulations yields consistent results, which show the same qualitative behavior as the measured conductivities.

Keywords: *Quantum dots, Quantum rings, Conductive atomic foce microscopy, Conductivity modelling, Transfer matrix method*

Povzetek

Lastnosti samosestavljenih InAs/InGaAs kvantnih pik in obročev smo preučili z mikroskopom na atomsko silo v prevodnem načinu (C-AFM). Dvodimenzionalne slike prevodnosti kvantnih obročev ter lokalne napetostno tokovne karakteristike razkrivajo nižjo prevodnost centralne jame v primerjavi z obodom in okolico v celotnem uporabljenem območju napetosti konice. Rezultat je presenetljiv, saj rezultati drugih študij kažejo, da je centralna jama območje z najvišjo relativno koncentracijo indija. Numerične simulacije "as-grown" vzorcev pokažejo, da je razlika v prevodnosti med centralno jamo ter obodom odvisna od napetosti na konici mikroskopa, kar je neskladno z eksperimentalnimi rezultati. Upoštevati je potrebno izpostavljenost vzorcev zraku, ki povzroči oksidacijo vrhnjih plasti. Z vključitvijo oksidirane plasti v numerične simulacije dobimo konsistentne rezultate, ki se kvalitativno ujemajo z eksperimentalnimi.

Ključne besede: *kvantne pike, kvantni obroči, mikroskop na atomsko silo v prevodnem načinu, modeliranje prevodnosti, metoda prenosnih matrik*

"Reality is whatever refuses to go away when I stop believing in it."
Philip K. Dick

Contents

Introduction

The intense progress of semiconductor electronics over the last few decades has revolutionized our everyday lives. Recently, integrated circuits, sensors, lasers, and other devices based on semiconductor nanostructures are permeating such diverse fields as photovoltaics, quantum computing, and biology. The small size of these strucutres gives them unique electronic and optical properties.

Recent advances in the epitaxial growth of semiconductor nanostructures with techniques such as molecular beam epitaxy (MBE) make it possible to form self-assembled nanostructures of various geometries. For years, quantum dots (QDs) have epitomized such structures, but recently, much attention has also been dedicated to torus-volcano shaped quantum rings (QRs) which are formed when QDs are capped in appropriate conditions with a few nanometers of the substrate material, followed by an annealing step at the growth temperature. Just like self-assembled QDs, QRs possess atomlike properties, making them candidates for future device applications in optoelectronics and quantum computing. On the other hand, their ring topology allows the observation of quantum-interference phenomena like the Aharonov-Bohm effect. While common characterization techniques such as photoluminescence and capacitance spectroscopy are useful in probing ensembles of QDs and QRs, scanning probe microscopy techniques become more advantageous when individual QDs and QRs are to be investigated.

This thesis focuses on InAs/GaAs QDs and QRs studied by conductive atomic force microscopy (C-AFM). The C-AFM technique allows for the surface topography and conductivity to be acquired simultaneously. A C-AFM tip enables current flow between tip and sample under applied bias. The local conductivity is governed by the height of the Schottky barrier between tip and sample, which in turn depends on the sample's top layer composition. Previous work that focused on C-AFM studies of InAs QDs has established that QDs are much more conducting than the wetting layer (WL) due to the lower Schottky barrier of InAs-rich regions. Measuring the local conductivity, one can thus obtain information about the sur-

face composition of such structures, the focus here being the In content variation between the capping layer, the rim, and the central hole of the QR.

Outline

Chapter 1 gives a brief introduction to quantum dots and rings. It describes their properties and potential applications and also various methods for fabricating QDs and QRs. The focus is on fabrication of structures via evaporation in ultra-high vacuum. The mechanisms of QD and QR formation are explained.

In Chapter 2, the instrumentation and techniques employed in this thesis are presented, namely, the molecular beam epitaxy (MBE) growth technique and the basic principles of atomic force microscopy (AFM) and conductive atomic force microscopy (C-AFM).

Chapter 3 describes the techniques used for numerical simulations of local current-voltage (I-V) spectra. The theory behind self-consistent Poisson-Schrödinger simulations is briefly outlined, followed by a description of the transfer matrix method (TMM) that is used to calculate the transmission coefficient of an arbitrarily shaped potential.

In Chapter 4, measurements of local I-V curves, C-AFM topography and current maps of QDs and QRs are presented. The discussion motivates the hypothesis that a surface oxide needs to be considered in the interpretation of the results in the case of QRs [1].

Chapter 5 deals with the numerical simulations of local I-V spectra. It describes the process and the results of numerical simulations for both the unoxidized and oxidized QR I-V spectra and includes the discussion of the results.

[1] The results on QRs described in Chapters 4 and 5 have been published as T. Mlakar, G. Biasiol, S. Heun, L. Sorba, T. Vijaykumar, G. U. Kulkarni, V. Spreafico, and S. Prato, Appl. Phys. Lett. **92** (2008) 192105.

Acknowledgments

I wish to thank the people at TASC who made this thesis possible: Stefan Heun for his continuing guidance and help with the research and writing of the thesis, Lucia Sorba for kindly giving me the oportunity to work in the AMD lab, Giorgio Biasiol for growing the samples and for helpful discussions of the results, and Daniele Ercolani for patiently teaching me everything I know about semiconductor processing. I also extend my gratitude to Stefano Prato and Vittorio Spreafico of APE Research for providing the AFM system and offering me technical support. To my loved ones, thank you for your patience.

Chapter 1

Quantum dots and rings: State-of-the-art

1.1 Quantum dots

A quantum dot (QD) is a semiconductor structure of a size that is comparable to the Fermi wavelength in all three spatial directions and which is able to confine electrons. Due to the small size, the energy spectrum of the dot becomes discrete. QDs are thus also called "artificial atoms" [1] since they exhibit similar properties: both have a discrete energy spectrum and can bind a small number of electrons. The similarity between atoms and QDs means that QDs exhibit a variety of quantum phenomena, such as charging effects including Coulomb blockade [2]. The confinement of electrons also greatly affects the optoelectronic properties of such materials compared with their bulk counterparts. As a result, semiconductor QDs show great promise for optoelectronic devices, where performance greatly depends on the shape, size, and material microstructure.

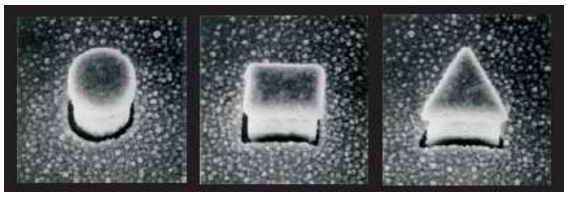

Figure 1.1: 'Pillar' quantum dots, fabricated using a top-down approach [2].

Nevertheless, there are some differences between atoms and QDs. In contrast to atoms, the confinement potential in quantum dots does not necessarily show

spherical symmetry. In addition, the confined electrons do not move in free space, but in the semiconductor host crystal. The quantum dot host material, in particular its band structure, does therefore play an important role for all quantum dot properties. Typical energy scales, for example, are of the order of 10eV in atoms, but only few meV in QDs. Unlike in atoms, the energy spectrum of a quantum dot can be engineered by controlling the geometrical size, shape, and the strength of the confinement potential.

Quantum dots with a nearly spherical symmetry, or flat quantum dots with nearly cylindrical symmetry, can show shell filling according to the equivalent of *Hund's rules* for atoms. In atomic physics, Hund's rule states that an atomic shell is first filled with electrons of parallel spin until the shell is half full. After that, filling continues with anti-parallel spins. In the case of two-dimensional artificial atoms (as is the case for the 'pillar' QDs shown in Fig. 1.1), the second shell is half filled when $N = 4$. Half filling of the third and fourth shells occurs for $N = 9$ and 16, respectively. These phenomena can be summarized in a periodic table for two-dimensional elements (Fig. 1.2). The rows are shorter than those for three-dimensional atoms due to the lower degree of symmetry.

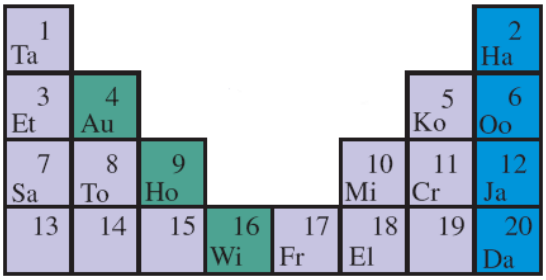

Figure 1.2: A periodic table of two-dimensional elements - quantum dots [2]. The elements are named after the members of the team that fabricated and characterized the QDs.

Apart from QD pillars shown in Fig. 1.1, which are fabricated using a top-down approach, confinement of electrons can be achieved in other ways. One possibility is to define metallic electrodes on top of a semiconductor heterostructure by means of electron beam lithography (Fig. 1.3). The heterostructure is fabricated in such a way that the electrons within are already confined in two dimensions, so when a negative bias is applied to the electrodes, an electrostatic potential is created which confines the electrons in all three directions.

Finally, probably the most common way of fabricating QDs is by means of

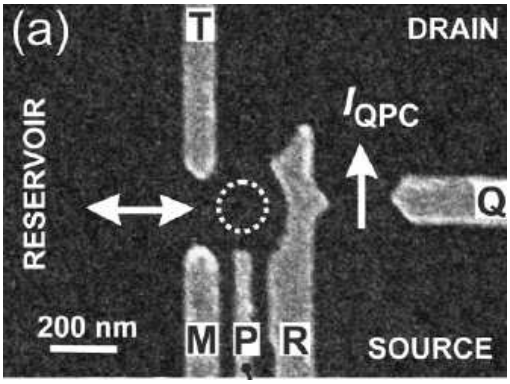

Figure 1.3: Scanning electron micrograph of an electrostatically defined quantum dot [3].

evaporation in ultra high vacuum (UHV) which forms the so called self-assembled QDs (Fig. 1.4), which are the topic of this text.

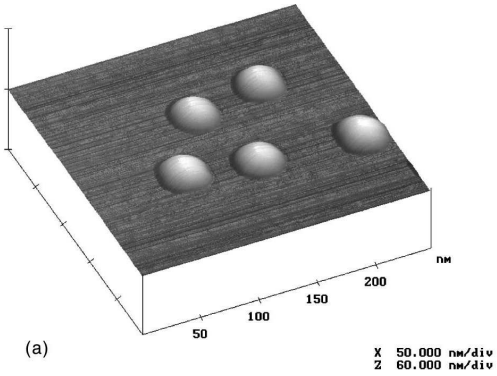

Figure 1.4: Atomic force micrograph of self-assembled quantum dots [4].

1.1.1 Fabrication of self-assembled Quantum Dots

Self-assembly of quantum dots via epitaxy techniques is realized by depositing a small amount (a few monolayers) of a material on a substrate. When a material is deposited onto a surface consisting of a different material, the deposited material arranges itself in such a way that it minimizes the surface energy. Surface energy can be described as the interaction between the forces of cohesion and the forces of adhesion. This balance of forces is given by the Young equation

$$\gamma_{SV} = \gamma_{SL} + \gamma_{LV} \cos \Theta \tag{1.1}$$

where γ_{SV}, γ_{SL}, and γ_{LV} are the interfacial tensions between the solid and the vapor, the solid and the liquid, and the liquid and the vapor, respectively (see Fig. 1.5). Θ is the contact angle that the drop makes with the surface in equilibrium (also known as *wetting angle*). An example of a large contact angle can be observed in the macroscopic world in the case of water droplets deposited on hydrophobic surfaces.

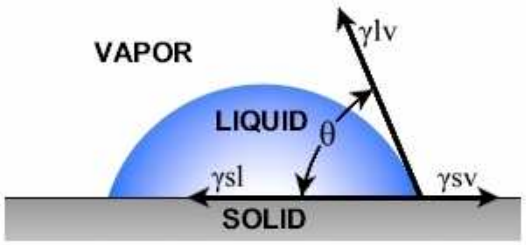

Figure 1.5: The balance of surface forces between all three phases [5].

Depending on the magnitude of the respective interface tensions, three different cases can be distinguished. On a higly reactive surface, the following inequality would hold

$$\gamma_{SV} \geq \gamma_{SL} + \gamma_{LV} \tag{1.2}$$

The wetting angle Θ is equal to 0 or undefined and thus the material is said to wet the surface. In the oposite case, when we have

$$\gamma_{SV} \leq \gamma_{SL} + \gamma_{LV}, \tag{1.3}$$

the deposited material does not wet the (poorly reactive) surface, instead it forms droplets with a finite contact angle Θ. The third possibility is to have a metastable equilibrium, where

$$\gamma_{SV} \approx \gamma_{SL} + \gamma_{LV}. \tag{1.4}$$

Depending on which of the above mentioned conditions holds, three epitaxial growth modes are possible: Frank-van der Merve mode, Volmer-Weber mode and Stranski-Krastanov mode (Fig. 1.6). Self-assembled QDs are formed via the metastable equilibrium Stranski-Krastanov (SK) mode.

The formation of 3D islands via SK mode can also be interpreted in terms of relaxation of strain. In order to form self-assembled QDs, materials whose crystal lattice constant differs from the one of the substrate need to be deposited (i.e.

InAs on GaAs or Ge on Si). When the first layer of a *lattice-mismatched* material is deposited, the incoming atoms arrange according to the substrate lattice. However, since the substrate lattice parameter differs from the one of the incoming material, the monolayer is strained. The strain energy increases linearly with the deposited thickness, and at some critical thickness it will become too large. The strain will be relaxed, and energetically more favorable 3D islands will be formed. After island formation the surrounding surface still contains residual InAs that forms the so-called *wetting layer* - WL.

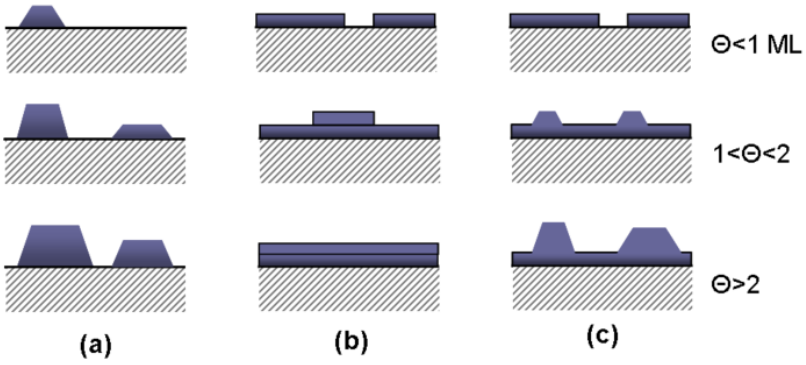

Figure 1.6: Cross-sectional views of the three primary modes of thin film growth: (a) Volmer-Weber, (b) Frank-van der Merwe, and (c) Stranski-Krastanov. Each mode is shown for several different amounts of surface coverage.

1.2 Quantum rings

Quantum rings are, as the name implies, ring-like nanostructures similar to quantum dots in that due to their small size they also provide charge carrier confinement and exhibit unique electronic and optical properties associated with their size and shape [6]. Quantum rings connected to leads also allow the observation of the Aharonov-Bohm effect [7], magnetic flux trapping and persistent currents, not affected by random scatterers [8, 9]. An example of a quantum ring fabricated by means of local anodic oxidation with a biased AFM tip is shown in Figure 1.7.

1.2.1 Quantum Ring fabrication

As mentioned above, ring-like quantum structures can be obtained by modifying a semiconductor surface to get the desired shape. This thesis focuses on self-

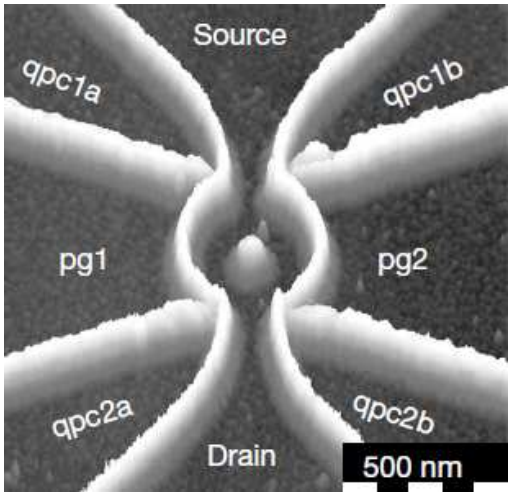

Figure 1.7: An AFM image of a quantum ring electronic device fabricated via local anodic oxidation [10].

assembled quantum rings, specifically InAs/GaAs QRs fabricated by molecular beam epitaxy. Self-assembled ring-like nanostructures can also be formed by other methods like droplet epitaxy [11].

InAs/GaAs QR formation is preceeded by first fabricating self-assembled InAs quantum dots on a GaAs surface as described in section 1.1.1. The InAs QDs are then capped with a thin layer of GaAs followed by annealing under As_2 flux [12]. Annealing of the partially capped dots causes strong material intermixing and redistribution towards the surrounding wetting layer (WL). In order to obtain a QR with an outer rim protruding out of the WL and a central hole below the WL level, the annealing time needs to be carefully controlled due to the fact that such a structure is not in thermodynamic equilibrium [13]. The evolution of capped InAs QDs with respect to annealing time is shown in Figure 1.8. As the annealing time is increased, an overall increase in the lateral size of the structures is observed. The QR structure forms after about 30s annealing time and later disappears and only a depression surrounded by a flat surface is observed after a certain annealing time. The same technique can also be used in transforming InAs/InP [14] and SiGe/Si QDs [15] to QRs.

Although a complete model of QR formation has not yet been developed, a few possible scenarios have been proposed. An example of a suggested mechanism is shown in Figure 1.9. Here it is assumed that the GaAs capping layer only covers the sides of the InAs QDs thus leaving the top of the dots exposed (Fig. 1.9a). This assumption is supported by the fact that no QR formation is observed

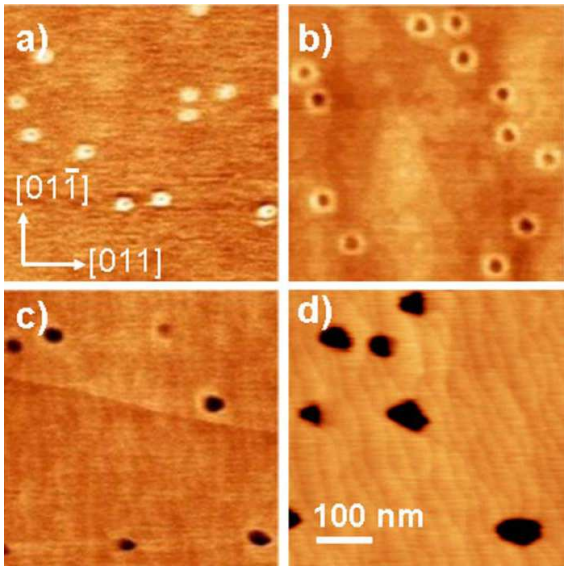

Figure 1.8: AFM images of InAs/GaAs QDs capped with 2nm GaAs followed by a) 0, b) 30, c) 120 and d) 360 s of annealing [13].

when the thickness of the GaAs capping layer is comparable or larger than the QD height [16]. At the annealing temperature (around 500°C) the mobility of In is higher than that of Ga, and so In diffuses outward and thus creates a hole at the site of the InAs dot. In the diffusion process the outgoing In is alloyed with the surrounding substrate atoms which reduces the material's mobility and finally leads to the formation of a ring-shaped nanoisland (Fig. 1.9c).

In addition to the diffusion process, there is strong evidence that additional mechanisms are needed to explain QR formation. The coexistence of QDs and completely formed QRs at certain growth conditions (as shown in Figure 1.10) suggests that QR formation is an abrupt process that diffusion alone cannot account for. Furthermore, the almost sharp QR edges also seem to be incompatible with an exclusively diffusion driven procees. As we have seen in the description of QD formation via Stranski-Krastanov growth, surface and interface forces are the main drivers of island formation. In uncapped QDs the balance is described by the Young equation (1.1). For partially capped dots the corresponding equation would be (Fig. 1.11b)

$$\gamma_{ac} = \gamma_{bc} \cos\Theta - \gamma_{ab} \cos\Theta, \tag{1.5}$$

which is incompatible with Eq. 1.1. We are left with an uncompensated Young force (Fig. 1.11c) given by [4]

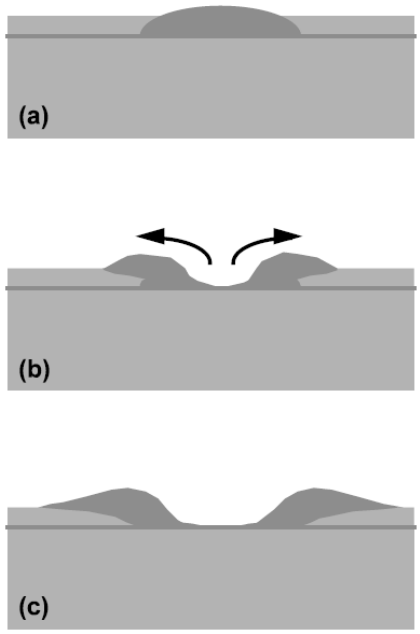

Figure 1.9: Diffusion-driven transformation from QDs to QRs. When the sample is annealed, the In-rich material (dark gray) diffuses away from the original location of the dot, whereas the less mobile Ga-rich material (light gray) remains mostly unchanged [17].

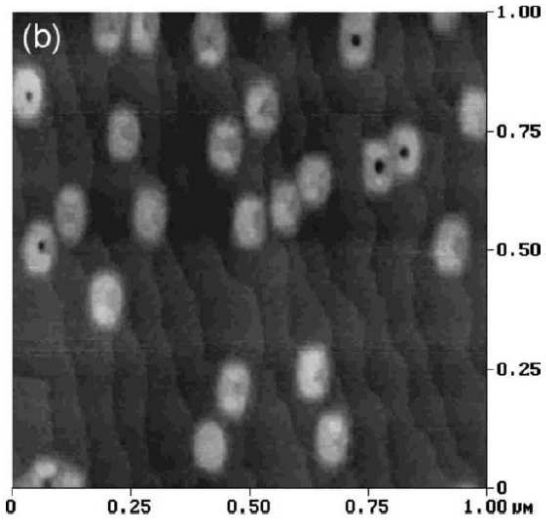

Figure 1.10: At certain growth conditions, not all islands exhibit a well-formed central hole, which suggests that the hole formation process is abrupt [17].

$$\Delta F = \gamma_{ab} \left(1 + \cos\Theta\right), \tag{1.6}$$

which causes the system to seek a new equilibrium by disintegrating the partially capped island and creating the central hole. We can therefore conclude that the QR formation is driven by at least two distinct processes. The In-rich material diffuses out of the uncapped dots, and the dewetting process establishes an equilibrium of interface forces.

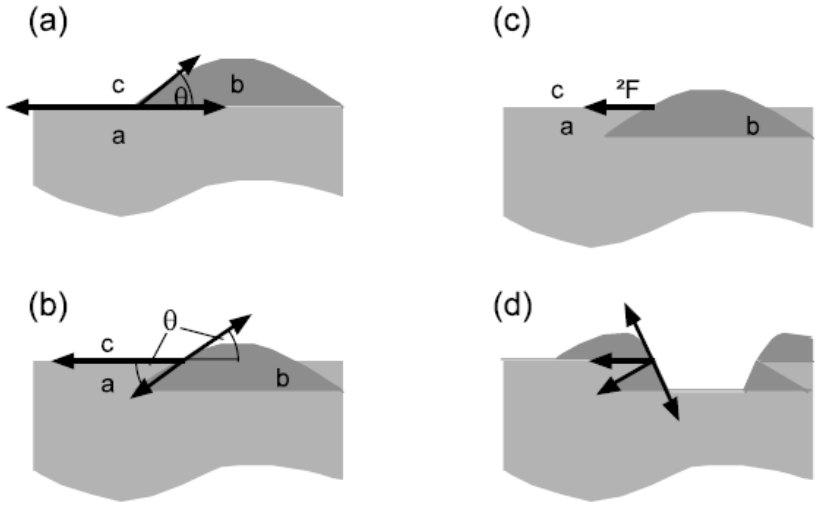

Figure 1.11: Model of QR formation via wetting droplet instability. a) balance of forces in an uncapped QD, b) balance of forces in partially capped QDs, c) an unbalanced net outward force, d) disintegration of the partially capped dots and formation of the central hole [17].

Chapter 2

Experimental

2.1 Molecular Beam Epitaxy

The self-assembled QDs and QRs used in this work are fabricated with a technique known as molecular beam epitaxy (MBE). MBE is performed in an ultra-high vacuum (UHV) chamber in order to minimize the amount of impurities incorporated into the evaporated material. In a solid-source MBE chamber ultra-high purity materials are heated up to the temperature where they begin to slowly sublimate or evaporate. The evaporated molecules or atoms are transported ballistically (if a high enough vacuum is achieved) to the heated substrate wafer where they are free to diffuse and are eventually incorporated into the growing material film. The technique allows the fabrication of high quality and high purity crystals, or in the case of simultaneous evaporation from more than one effusion cell, the formation of binary compounds or ternary alloys (i.e. GaAs or InGaAs), where the individual material contents are precisely controlled. Another advantage of MBE is the high control over deposited material thickness, since it allows monoatomic layer-by-layer growth with an accuracy even better than one monolayer ($\approx 0.3nm$). A schematic drawing of an MBE system is shown in Figure 2.1. The main components of an MBE system are:

- A stainless-steel growth chamber which holds the ultra-high vacuum. It is connected to the preparation chamber used for degassing the substrates before growth.

- The pumping system which lowers the pressure to values from 10^{-11} to 10^{-12} mbar in order to minimize the concentration of impurities.

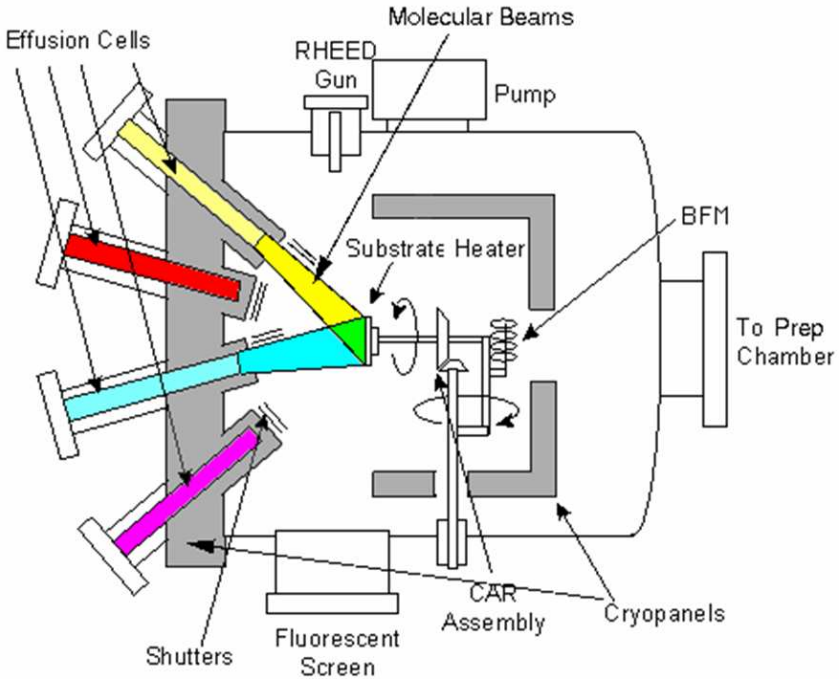

Figure 2.1: A schematic drawing of a MBE system.

- Liquid nitrogen cryopanels provide thermal isolation between different material cells and prevent material re-evaporation from chamber walls.
- Effusion cells contain the high-purity materials for evaporation. The cells are focused on the substrate and must provide high flux stability and uniformity. On-off switching of the flux is realized with pneumatic or mechanical shutters in front of the cells.

During epitaxial growth the atoms are physisorbed or chemisorbed on the surface where they can undergo different processes as shown in Figure 2.2. For III-V semiconductors the so-called *three temperatures method* [18] is used, where the substrate temperature is kept in between the evaporation temperatures of the III and V group source materials. Group III atoms have a lower vapor pressure compared to group V elements, therefore the typical effusion cell temperatures are lower for group V (around 300°C for As) than for group III (around 800°C and 900°C for In and Ga, respectively). The vapor pressure of group III elements is almost zero at the substrate temperature, which means that every impinging atom is chemisorbed to the surface. Group V atoms, on the other hand, are much more volatile due to the higher vapor pressure and are thus likely to re-evaporate. To compensate for this difference, the V/III beam flux ratio is usually kept much

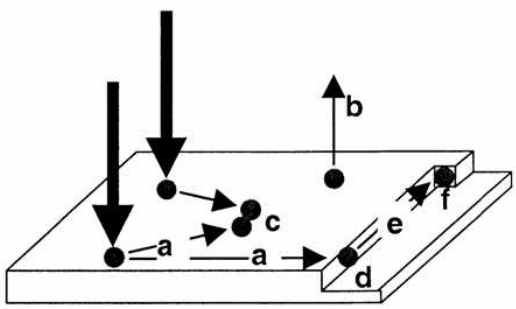

Figure 2.2: Surface elementary processes: a) surface diffusion, b) reevaporation, c) formation of clusters, d) incorporation at a step, e) edge migration, and f) incorporation at a kink.

higher than one. A high flux ratio, however, does not affect the one-to-one III-V element ratio in the crystal. It has been shown in the case of homoepitaxial growth of GaAs that As atoms do not stick to the surface if there are no Ga atoms available for bonding. The growth rate is thus controlled by the Ga flux [19]. For a growth rate of about $1\mu m/h$ the typical fluxes are $\sim 10^{16}$ atoms $cm^{-2}s^{-1}$ for group V and $\sim 10^{15}$ atoms $cm^{-2}s^{-1}$ for group III elements.

In order to monitor the growth rates, Reflection High Energy Electron Diffraction (RHEED) is used. The technique uses a high energy electron beam (up to 20keV) which impinges on the sample at an angle of a few degrees. A floures-cent screen captures the diffraction pattern. Because of the low angle of incidence the electrons are only scattered by the topmost atomic layers which results in a surface-sensitive diffraction pattern. By monitoring the oscillations of the zero order diffraction spot intensity we can infer the monolayer coverage during growth in real time (Fig. 2.3). Growth rates of InAs on GaAs, however, are difficult to obtain with this technique since the lattice mismatch between the materials results in 3D island formation. InAs growth rate is evaluated by measuring the growth rate of GaAs in an InGaAs sample combined with ex-situ determination of In content by X-ray diffraction.

The samples for the purpose of this thesis were grown in the MBE chamber at Laboratorio TASC INFM-CNR in Trieste (Fig. 2.4), which is primarily dedicated to the growth of high-mobility AlGaAs/GaAs heterostructures.

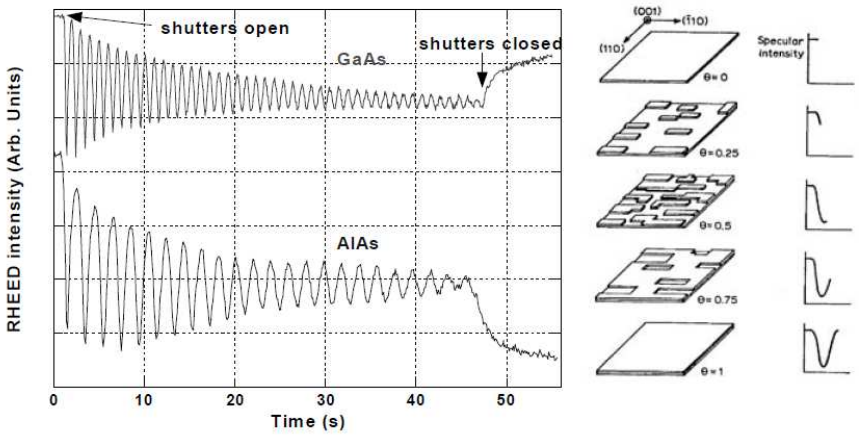

Figure 2.3: Left: an example of a RHEED oscillation measurement. Right: a schematic view of the relationship between the intensity of the RHEED signal and the monolayer coverage.

Figure 2.4: A photograph of the high-mobility MBE system in Laboratorio TASC INFM-CNR in Trieste.

2.2 Atomic Force Microscopy

The atomic force microscope (AFM) was introduced in 1986. The AFM was a new type of microscope that was able to obtain high resolution images of both conductive and insulating samples. The AFM is part of the scanning probe microscopes (SPMs) family. The operating principle of all SPMs is to form an image of surfaces using a sharp physical probe (tip) that scans the sample. An image of the surface is obtained by mechanically moving the probe in a raster scan of the specimen. The various SPMs differ in the parameter used to detect the tip-sample distance. In the case of AFM the distance is determined from the forces acting between the tip and the sample.

The forces that arise between the tip and the sample are [20]: (i) electrostatic or Coulomb interactions, (ii) polarization forces, (iii) quantum-mechanical forces, which give rise to covalent bonding and repulsive exchange interactions, and (iv) capillary forces that arise when the AFM is operated in a humid environment. The repulsive forces increase sharply as the tip-sample distance becomes comparable to the interatomic distances, while, when separating tip from sample, they drop to zero at tip-sample separation of about 0.3nm after which the interactions become attractive (see Fig. 2.5).

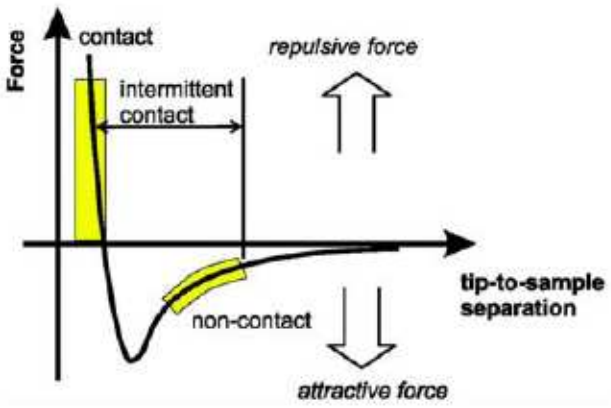

Figure 2.5: The relation betweent the force and tip-sample distance. Depending on the force, an AFM can be operated in one of three regimes: contact, intermittent contact, and non-contact mode.

The tip-sample interactions are usually described by a Lennard-Jones potential:

$$U(d) = 4\epsilon \left[\left(\frac{\sigma}{d}\right)^{12} - \left(\frac{\sigma}{d}\right)^{6} \right], \tag{2.1}$$

where d is the tip-sample distance, σ is the distance at which $U(\sigma) = 0$, and ϵ is the depth of the potential well. The derivative of Eq. 2.1 represents, to a first approximation, the force between tip and sample (see Fig. 2.5).

Since the introduction of the AFM, quite a few derivative techniques that are mainly focused on semiconductor characterization have been developed. Among these we find Scanning Capacitance Microscopy [21] and Scanning Spreading Resistance Microscopy [22] which are primarily used to image the distribution of dopant concentrations within semiconductors. The development of Kelvin Probe Force Microscopy [23] allows the detection of tip-surface contact potential differences. Further techniques include Electrostatic Force Microscopy which enables the detection of charges within dielectric films [24] and Conductive Atomic Force Microscopy (C-AFM). C-AFM differs from conventional AFM in that it allows highly sensitive current measurements of the sample through applying a bias to a conductive tip. Apart from conductivity and topography measurements performed in parallel, C-AFM can be utilized to locally modify surfaces and fabricate nanostructures by local anodic oxidation (LAO) [25]. LAO occurs in a humid enviroment when a water meniscus is formed between the tip and the sample. When a high enough bias is applied, the water molecules in the meniscus dissociate, and the OH^- ions migrate towards the sample surface where oxidation occurs (Fig. 2.6). The C-AFM technique will be presented in further detail later in this section.

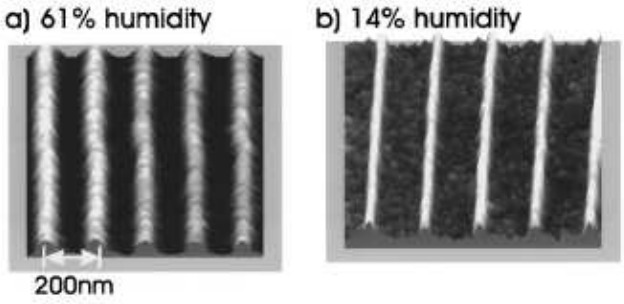

Figure 2.6: Modification of the sample surface via local anodic oxidation using a biased AFM tip [25].

2.2.1 Atomic Force Microscopy operation

The tip of an AFM is fixed to a cantilever and mounted on a carrier chip. As the tip interacts with the sample, the cantilever bends. This deflection is measured with a laser beam which is directed at the reflective backside of the cantilever. The laser beam is deflected by the cantilever onto a position sensitive photodetector (PSPD), see Fig. 2.7. A change in tip-sample force results in a change in the bending of the cantilever which causes the laser spot on the PSPD to move. The intensity of the signal measured by the PSPD is thus related to the force which the cantilever experiences. The piezo tube under the sample is used for fine movements in all three directions (x, y, z).

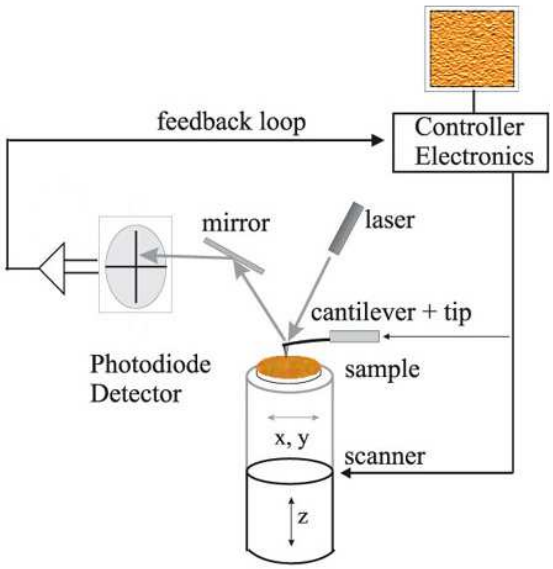

Figure 2.7: Schematic of an AFM system.

Two basic AFM operational modes are used: constant height and constant force mode. In constant height mode, the AFM tip is scanned on the sample at a fixed distance, and the sample topography is related directly to the cantilever bending. Constant height mode is more suitable for high scanning rates but the drawback is that the sample surface must not be corrugated too much. In constant force mode, the feedback loop acts on the piezo tube in order to keep the tip-sample force constant at a pre-set value. In this mode, the sample topography is given by the movements of the piezo.

From the point of view of interaction force, there are three possible regimes of AFM operation: contact, non-contact and intermittent contact. Each mode

corresponds to a specific region in the force-distance curve as shown in Fig 2.5. In contact mode (CM), the tip is touching the sample surface. The tip-sample interactions are repulsive with a magnitude of about 10^{-6} - 10^{-9} N. The short range repulsive forces allow imaging with a relatively high resolution, but on the other hand the sample surface can be damaged in the process. In non-contact mode (NCM), the tip-sample distance is 10 to 100 nm. Due to van der Waals interactions, the tip-sample force is attractive with a typical magnitude of about 10^{-9} - 10^{-12} N. In NC mode, the cantilever is caused to vibrate just above its resonance frequency. When the tip approaches the sample, the interactions cause a decrease in the resonance frequency which in turn results in a decrease of the amplitude of oscillation (Fig. 2.8a). The amplitude is monitored via a feedback loop in order to control (and read) the tip-sample distance. The interactions in NC mode are about 10^3 - 10^6 times lower than in contact mode and can thus be used to image very delicate samples such as organic films. On the other hand, the spatial resolution that can be achieved in NC mode is not as high as in contact mode, since NC mode is based on long-range van der Waals interactions.

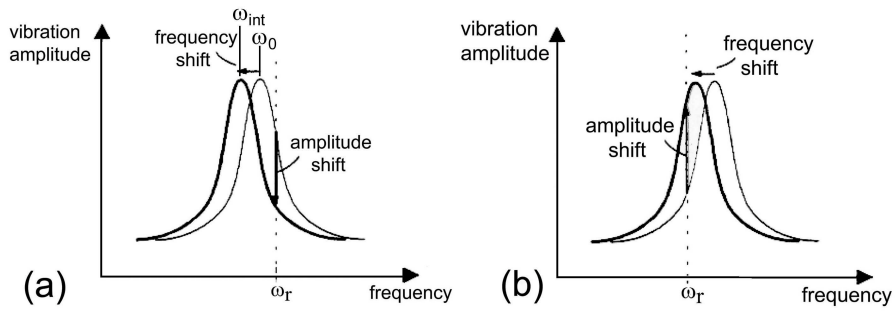

Figure 2.8: Frequency and amplitude shift of an AFM cantilever in a) non-contact mode and b) intermittent contact mode.

The intermittent contact mode (ICM) is similar to NCM, but in ICM the cantilever is vibrating at a frequency just *below* the resonance freqency. As the tip is brought closer to the sample, the interaction again causes a decrease in the resonance frequency which, in contrast to the NCM mode, now results in an increase in the vibration amplitude up to the point where the tip touches the sample surface. This in turn reduces the vibration amplitude back to the set value. As in NCM, the vibration amplitude is used to control the tip-sample distance. The spatial resolution of ICM is comparable to that of CM while the interaction strength lies between CM and NCM.

2.2.2 Conductive Atomic Force Microscopy

As mentioned before, a C-AFM system allows to obtain simultaneous topography and conductivity measurements [26, 27]. Unlike in an STM, the topography information is completely separated from the electrical part in a C-AFM. To obtain the additional electrical signal, a voltage is applied between the conductive AFM tip and the sample. The bias is usually applied to the sample. The resulting current is measured using a highly sensitive amplifier as a current-to-voltage converter as close to the tip as possible to minimize noise. Depending on the current range to be measured, an operational amplifier (OA) based electrometer or a diode based logarithmic amplifer can be used. A typical C-AFM scheme based on an OA is shown in Figure 2.9. Additionally, the amplifier gain needs to be chosen according to the range of measured currents of a particular material. The current ranges can be from a few fA up to hundreds of nA. The measured samples are usually mounted on the sample holder with conductive silver paste or with a durable conductive two component epoxy glue. In case the samples need to be baked (which would destroy the conductivity of silver paste and epoxy glue), mechanical clamps can be used.

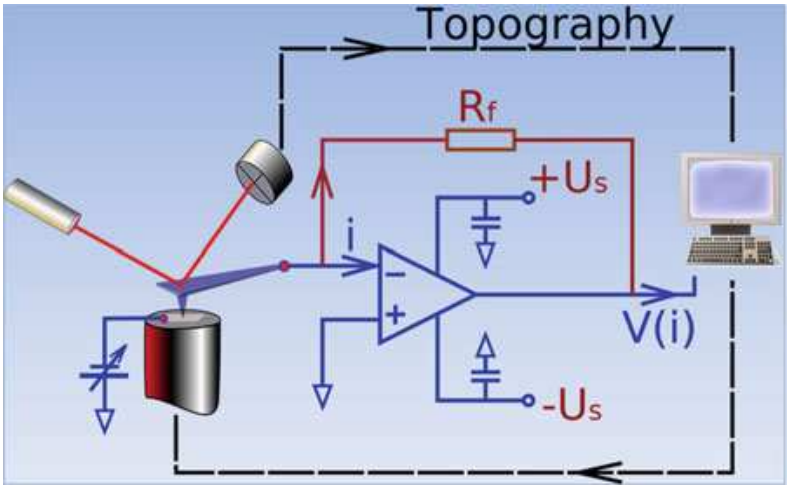

Figure 2.9: The setup of a C-AFM system [28]. The current is converted to voltage according to $V(i) = i \cdot R_f$.

The quality of a C-AFM measurement also depends on the conductive tip properties. Among the various conductive probes for C-AFM, the ones coated with wear-resistive conductive materials are usually preferred due to their electrical properties and stability of tip geometry. Standard coatings include Au, TiN, PtIr and heavily doped diamond. A SEM image of a diamond coated probe is shown in Figure 2.10. In choosing the probe (diamond vs. metal-coated) there is a trade-off

between resistivity (lower for metal-coated probes) and resistance to wear (higher for diamond-coated tips). Additionally, the radius of curvature is smaller for metal-coated tips (typically 35 nm compared to 100 nm for diamond-coated probes [28]) which also needs to be taken into account depending on the roughness of samples under investigation. In the case of barrier formation at tip-sample contact, the work functions of coating materials also need to be considered.

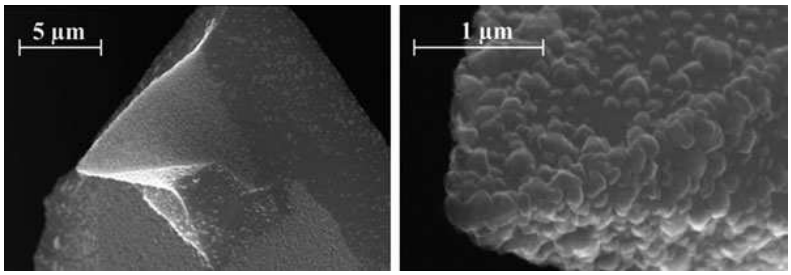

Figure 2.10: SEM image of a diamond-coated probe [28].

The C-AFM technique can be used to investigate materials in a variety of ways. As mentioned, 2D current maps can be obtained together with topography. For this, a constant voltage is applied to the sample and the tip is scanned across the surface in contact mode. In this way we obtain two images of the same area, one with topographical and one with electrical information which enables us to study the correlation between the two. Apart from 2D maps, one can investigate local properties of a material by measuring individual current-voltage (I-V) curves. In this case, the tip is brought into contact with the sample, with the scanner off, and the voltage to the tip or sample is ramped to a predefined value in a certain time. In order to obtain information on the statistical distribution, several I-Vs are usually acquired in several spots on the sample surface. A similar experiment can be performed to determine the electric stress influence if instead of the voltage ramp we apply a constant voltage for a period of time. With this approach, the current versus time and as a function of applied voltage can be measured, and information about the influence of current on the sample is obtained.

Using all the mentioned approaches, the C-AFM technique has thus far been used for investigations of a wide range of materials. Apart from the study of quantum dots and rings which will be discussed in the next section, materials such as dielectrics [29], ferroelectrics [30], organic materials [31], and even carbon nanotubes have been investigated with C-AFM [32].

The C-AFM system used in this thesis is shown in Figure 2.11. It is an APE

Research AFM-R80 system that enables us to perform C-AFM measurements using an amplifier with a gain of $10^{12}V/A$. The noise level of the current measurements can be as low as 10fA. When performing C-AFM measurements, the AFM system was kept in a glovebox under a nitrogen atmosphere. This enabled us to minimize the humidity and thus prevent local anodic oxidation of the sample surface.

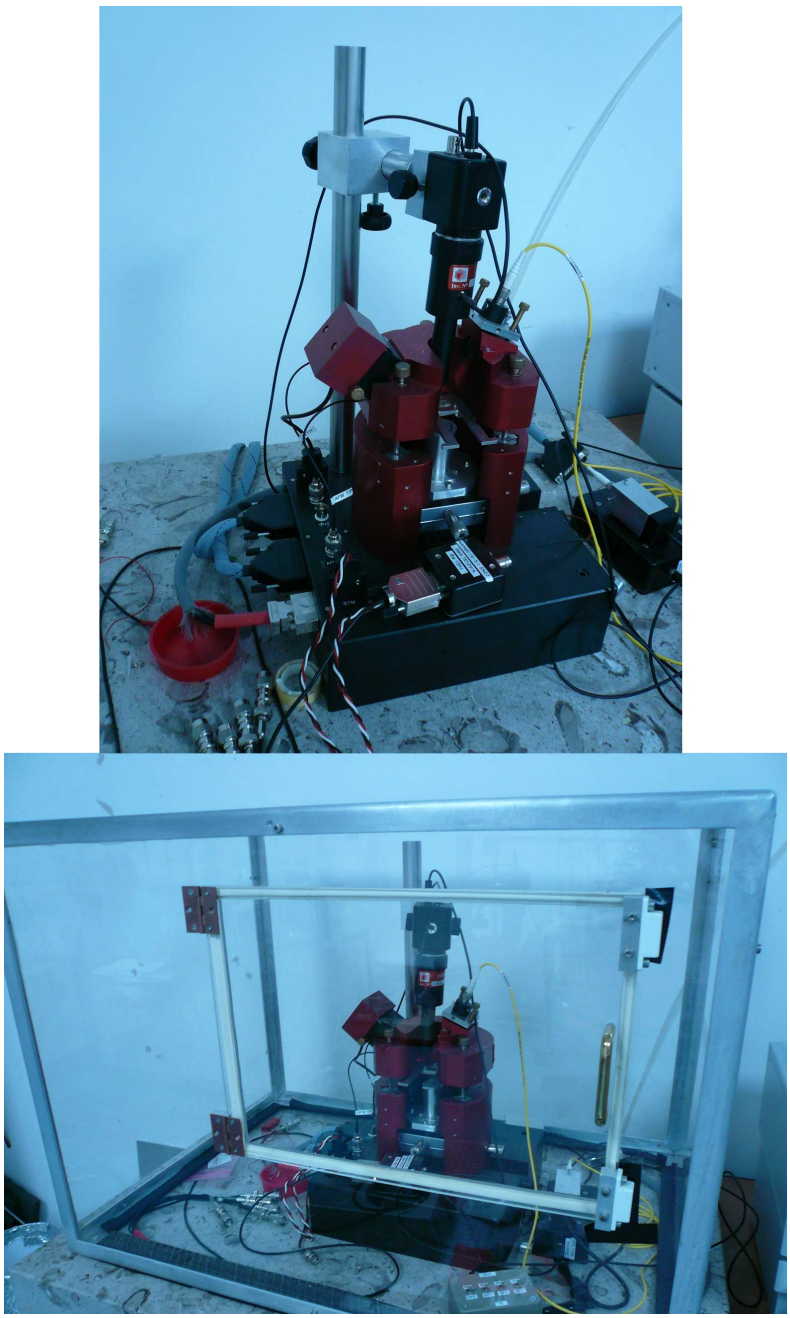

Figure 2.11: Top: an APE Research AFM-R80 system equipped with an amplifier with a gain of $10^{12}V/A$ and a current noise of about 10fA. Bottom: for the C-AFM measurements, the AFM system is placed under a glovebox in a nitrogen atmosphere in order to minimize humidity and thus avoid local anodic oxidation.

Chapter 5

Numerical techniques

In addition to acquiring C-AFM topography and current maps we also performed local current-voltage (I-V) spectroscopy measurements. The measured I-V spectra are compared to theoretical models for different sample structures. Numerical calculations of I-V spectra are based on the Tsu-Esaki formalism, which describes the net current density flowing from a metal to a semiconductor through a potential barrier [33]. In the 1D approximation where current flows only in the x direction, the net current density assumes the form [34]

$$J = \frac{qm^* k_B T}{2\pi^2 \hbar^3} \int_{E_{min}}^{\infty} T\left(E_x\right) \cdot \ln \left[\frac{1 + \exp\left(\frac{E_{F,M} - E_x}{k_B T}\right)}{1 + \exp\left(\frac{E_{F,S} - E_x}{k_B T}\right)} \right] dE_x, \tag{5.1}$$

where $T\left(E_x\right)$ is the transmission coefficient for the electrons impinging on the potential barrier as a function of the incoming electron energy and $E_{F,M}$ and $E_{F,S}$ are the electron quasi-Fermi levels in the metal and the semiconductor, respectively. E_{min} is the minimum energy at which tunneling can occur. In order for the net current to be calculated, we need to know the transmission coefficient which in turn depends on the shape of the potential barrier. The numerical procedure is thus as follows: given a certain sample structure and surface (metal) bias we calculate the shape of the potential barrier (see Section 3.1); once the potential is known, we calculate the transmission coefficient as a function of incoming particle energy (see Section 3.2); using Eq. 5.1, finally we calculate the net metal-semiconductor current density for a certain voltage bias of the metal; we repeat the procedure for other values of surface bias and combine the results into an I-V spectrum. It should be stressed that the quantity being simulated is current density, whereas the quantity measured is total local current. Nevertheless, the simulations provide

crucial qualitative estimates of the relative conductivities of different sample regions. The numerical techniques employed in this procedure are presented in the following subsections.

5.1 Poisson-Schrödinger simulations

Poisson-Schrödinger simulations are a frequently used tool to estimate energy bands, carrier densities, distribution of charge in the structures, and number of populated subbands in various semiconductor structures. The conventional numerical approach is to obtain a self-consistent, one-dimensional solution of the Schrödinger and Poisson equations using the finite-difference method where real space is divided into discrete mesh points. The 1D Poisson solver developed by Gregory Snider, used in this thesis, employs the above-mentioned approach using a non-uniform mesh size [35, 36]. The basic equations used are the one-dimensional, one electron Schrödinger equation

$$-\frac{\hbar^2}{2}\frac{d}{dx}\left(\frac{1}{m^*(x)}\frac{d}{dx}\right)\psi(x) + V(x)\psi(x) = E\psi(x), \tag{5.2}$$

where ψ is the wave function, E is the energy, V is the potential energy, $\hbar$ is the Planck constant divided by 2π and m^* is the effective mass, and the one-dimentional Poisson equation

$$\frac{d}{dx}\left(\epsilon_s(x)\frac{d}{dx}\right)\phi(x) = \frac{-q\left[N_D(x) - n(x)\right]}{\epsilon_0}, \tag{5.3}$$

where ϵ_s is the dielectric constant, ϕ is the electrostatic potential, N_D is the ionized donor concentration, and n is the electron density distribution. We set the potential energy V to be equal to the conduction band energy in order to find the electron distribution in the conduction band. The relation between the potential energy V and the electrostatic potential ϕ in a quantum well with an arbitrary potential energy profile is

$$V(x) = -q\phi(x) + \Delta E_c(x), \tag{5.4}$$

where $\Delta E_c(x)$ is the pseudopotential energy due to the band offset at the heterointerface. The relation between the wavefunction $\psi(x)$ and the electron density $n(x)$ is given by

$$n(x) = \sum_{k=1}^{m} \psi_k^*(x)\psi_k(x)n_k, \tag{5.5}$$

where m is the number of bound states, and n_k is the electron occupation for each state. The latter can be obtained from

$$n_k = \frac{m^*}{\pi\hbar^2} \int_{E_k}^{\infty} \frac{1}{1 + \exp\left(E - E_F\right)/kT} dE, \tag{5.6}$$

where E_k is the eigenenergy.

A self-consistent solution for Eqs. 5.2 and 5.3 is obtained using an iterative process. Given an initial approximation for the potential $V(x)$, the wave functions, and the eigenenergies E_k we can calculate $n(x)$ using equations 5.5 and 5.6. The resulting $n(x)$ together with the known donor concentration N_D are used in Eq. 5.3 to get $\phi(x)$ from which we get the new potential $V(x)$ using Eq. 5.4. The process is continued iteratively until a self-consistent solution with the desired accuracy is obtained.

5.2 Transfer matrix method

Once the shape of the potential barrier is known, we approximate the transmission coefficient for the electrons incident on the potential barrier using the transfer matrix method (TMM). TMM is a numerical technique which can be used to calculate the transmission and reflection coefficients of an arbitrarily shaped surface potential. The basic idea is to divide the surface potential into layers and approximate each layer with a constant potential (Fig. 5.1) for which the solution of the one-dimensional, time-independent Schrödinger equation is known. By applying continuity conditions for wavefunctions and their derivatives on layer interfaces, the relation between the wavefunctions of the incoming electrons and the electrons on the other side of the potential barrier can be obtained [37].

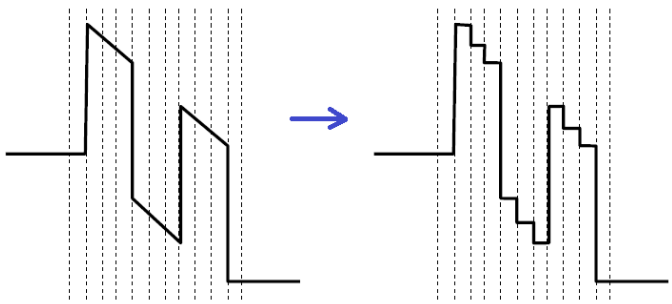

Figure 5.1: An arbitrary surface potential is approximated with adjacent layers of constant potential for which the transmission coefficient can be obtained analytically.

If we consider a single constant potential jump of height V at $x = 0$, the solution of the stationary Schrödinger equation in region 1 ($x < 0$) can be written as

$$\Psi_1(x, k_1) = A_1 e^{ik_1 x} + B_1 e^{-ik_1 x} \tag{5.7}$$

and in region 2 ($x > 0$) as

$$\Psi_2(x, k_2) = A_2 e^{ik_2 x} + B_2 e^{-ik_2 x}, \tag{5.8}$$

where $k_1 = \sqrt{2mE}/\hbar$ and $k_2 = \sqrt{2m(E-V)}/\hbar$. By applying the continuity conditions at $x = 0$

$$\Psi_1(0) = \Psi_2(0) \tag{5.9}$$

and

$$\frac{d\Psi_1}{dx}(0) = \frac{d\Psi_2}{dx}(0), \tag{5.10}$$

we obtain the relations

$$A_1 e^{ik_1 x} + B_1 e^{-ik_1 x} = A_2 e^{ik_2 x} + B_2 e^{-ik_2 x} \tag{5.11}$$

$$ik_1 A_1 e^{ik_1 x} - ik_1 B_1 e^{-ik_1 x} = ik_2 A_2 e^{ik_2 x} - ik_2 B_2 e^{-ik_2 x} \tag{5.12}$$

Written in matrix form, the relations become

$$\begin{bmatrix} e^{ik_1 x} & e^{-ik_1 x} \\ ik_1 e^{ik_1 x} & -ik_1 e^{-ik_1 x} \end{bmatrix} \begin{bmatrix} A_1 \\ B_1 \end{bmatrix} = \begin{bmatrix} e^{ik_2 x} & e^{-ik_2 x} \\ ik_2 e^{ik_2 x} & -ik_2 e^{-ik_2 x} \end{bmatrix} \begin{bmatrix} A_2 \\ B_2 \end{bmatrix} \tag{5.13}$$

The above can be rewritten as

$$T(x, k_1) \begin{bmatrix} A_1 \\ B_1 \end{bmatrix} = T(x, k_2) \begin{bmatrix} A_2 \\ B_2 \end{bmatrix} \tag{5.14}$$

$\Leftrightarrow$

$$\begin{bmatrix} A_2 \\ B_2 \end{bmatrix} = T^{-1}(x, k_2)\, T(x, k_1) \begin{bmatrix} A_1 \\ B_1 \end{bmatrix} \tag{5.15}$$

where we denoted the 2×2 matrices with $T(x, k_1)$ and $T(x, k_2)$, respectively. By multiplying the matrices we get the transfer matrix TM, which relates the coefficients of the wavefunctions in region 1 with those in region 2:

$$TM(x, k_1, k_2) = T^{-1}(x, k_2)\, T(x, k_1) \tag{5.16}$$

By repeating the procedure for all interfaces of adjacent constant potential regions, we get

$$\begin{bmatrix} A_N \\ B_N \end{bmatrix} = TM(x, k_{N-1}, k_N)\, TM(x, k_{N-2}, k_{N-1}) \ldots TM(x, k_1, k_2) \begin{bmatrix} A_1 \\ B_1 \end{bmatrix} \tag{5.17}$$

By again multiplying the matrices in Eq. 5.17 and setting $B_N = 0$ (we take the particles to be incoming from the left-hand side only), we get

$$\begin{bmatrix} A_N \\ 0 \end{bmatrix} = TT \begin{bmatrix} A_1 \\ B_1 \end{bmatrix} = \begin{bmatrix} t_{11} & t_{12} \\ t_{21} & t_{22} \end{bmatrix} \begin{bmatrix} A_1 \\ B_1 \end{bmatrix}, \tag{5.18}$$

where TT is the global transfer matrix which relates the wavefunction of the incoming particles with the wavefunction of the reflected and the transmitted particles. From the above relation we get

$$t_{21} A_1 + t_{22} B_1 = 0 \tag{5.19}$$

and

$$A_N = t_{11} A_1 + t_{12} B_1 = A_1 \left(t_{11} - \frac{t_{12} t_{21}}{t_{22}} \right) \tag{5.20}$$

The reflection and transmission coefficients are then

$$R = \left| \frac{B_1}{A_1} \right|^2 = \left| \frac{t_{21}}{t_{22}} \right|^2 \tag{5.21}$$

$$T = \left| \frac{A_N}{A_1} \right|^2 = \left| t_{11} - \frac{t_{12} t_{21}}{t_{22}} \right|^2 . \tag{5.22}$$

The transmission coefficient is input into Eq. 5.1 to obtain a value of the net current density, which represents a point of the I-V spectrum. The procedure is repeated for different surface bias values until a full I-V curve is obtained. Numerical calculations of transmission coefficients and net current densities were performed using *Mathematica* [38]. The routines are presented in Appendix A.

Chapter 6

C-AFM of quantum dots and quantum rings

6.1 C-AFM of quantum dots

Initially, quantum dot samples were mapped with C-AFM. To avoid local anodic oxidation of the sample surface, the C-AFM system was placed under a glovebox in a controlled nitrogen atmosphere, keeping the relative humidity at around 14% for all C-AFM measurements. The samples were attached to a conductive sample holder with conductive silver paste. Additionally, indium contacts were made between the sample surface and the sample holder to provide better conductivity for C-AFM measurements.

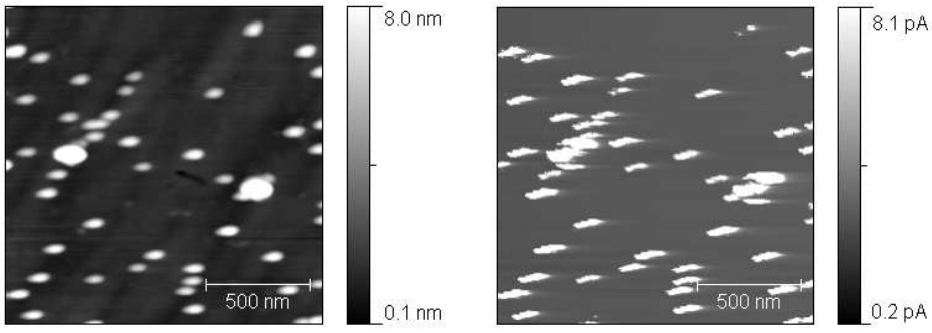

Figure 6.1: Topography (left) and current (right) maps of QDs (sample no. HM 1926d), measured simultaneously with a tip bias of -2V. Image size is $1.5\mu m \times 1.5\mu m$, tip scan speed is $1\mu m/s$. Maps were acquired using a Ti-Pt coated n-doped silicon tip (NSG14 by MicroMasch), with a tip-sample force of 30nN.

Previous work that focused on C-AFM studies of QDs has established that InAs QDs are much more conducting compared to the surrounding wetting layer due to the lower Schottky barrier of InAs-rich regions [39–41]. The higher conductivity of InAs is a consequence of a lower band-gap (0.354eV at 300K) compared to that of GaAs (1.424eV at 300K). The topography and current measurements of QDs are shown on Fig. 6.1. The QDs are 5-8nm high with a diameter in the range of 100-150nm. Consistent with reports in literature, the conductivity of QDs is higher than that of the WL. When comparing the topography and current images, we notice that the shape of the QDs seen in the topography image is circular - the elongation of the QD shape in the current image is an artefact due to saturation of the amplifier.

6.1.1 I-V measurements

In addition to current mapping, local I-V spectroscopy on QDs was also performed. In this case, the tip is brought into contact with the sample at a specific point on the surface, and the voltage is ramped while the current is being collected. The results are shown in Fig. 6.2. Both curves exhibit rectifying behaviour due to the Schottky barrier. Comparing the QD and WL I-V curves confirms the existance of a higher Schottky barrier in the WL due to the lower In content. The discrepancy in the absolute current values between Fig. 6.1 and Fig. 6.2 is due to the different AFM tip-sample force.

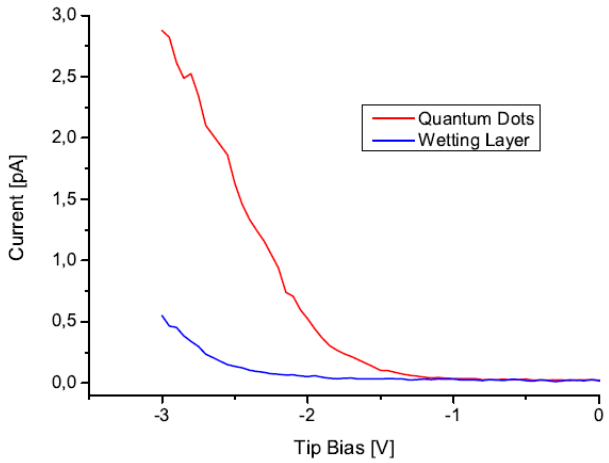

Figure 6.2: I-V spectra of InAs QDs and of the surrounding WL. The red line is an average of 10 measured I-V curves and the blue line an average of 8 I-V curves. The curves were acquired with a resolution of 0.05V and a sweep rate of 1V/s.

6.2 C-AFM of quantum rings

As next step, topography and current maps of QRs were measured. As with the QD samples, the measurements were performed in a controlled nitrogen atmosphere. The results measured on sample no. HM 2227 are presented in Fig. 6.3. Topography measurements and cross-sectional profiles such as the one shown in Fig. 6.5 reveal that QRs have a typical outer diameter of about 150nm with a rim height of about 0.5nm above the wetting layer and the central hole about 2nm deep below the rim (Fig. 6.4). The most significant feature exhibited in the current map in Fig. 6.3 is the lower conductivity of the central QR hole compared to the rim and capping layer. The QRs in sample HM 2227 were fabricated by depositing 2nm of GaAs on QDs that were formed with the deposition of 2 monolayers (ML) of InAs on a doped GaAs substrate at 550°C. Different regions of the sample (1/4 of a 2 inch wafer) were measured and yielded similar qualitative results. C-AFM measurements were also performed on sample HM 2152, where QRs are formed on QDs obtained with the deposition of 1.5 ML of InAs. Apart from n-doped silicon tips used for obtaining Fig. 6.3, Ir-Pt coated tips were also used and yielded similar results. In all experiments the samples were conducting for tip bias values larger than -2V and all exhibited higher conductivity of the QR rim compared to that of the QR central hole. Typical tip-sample forces in our measurements were 20-60nN and scan speeds in the 200-1000nm/s range were used.

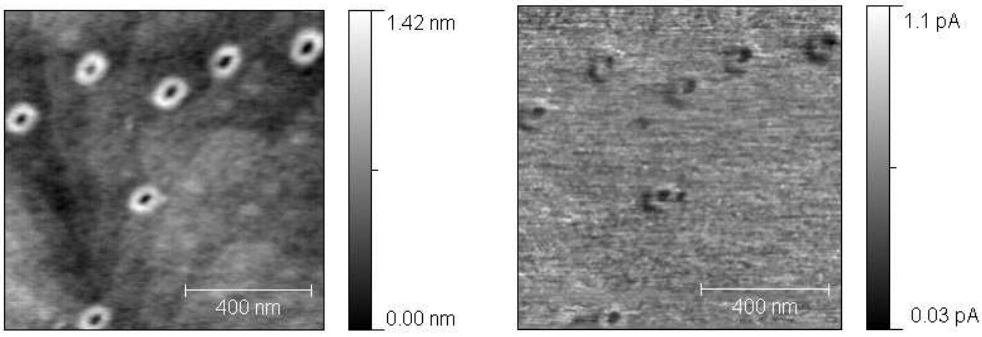

Figure 6.3: Topography (left) and current (right) maps of QRs, measured simultaneously with a tip bias of -2.5V (sample no. HM 2227). Image size is $1\mu m \times 1\mu m$, tip scan speed is $1\mu m/s$. Maps were acquired using a n-doped silicon tip (CSG10 by NT-MDT), with a tip-sample force of 30nN.

A closer look at the conductivity of different QR regions is given in Fig. 6.5. The figure shows cross-sections of topography and current obtained through the

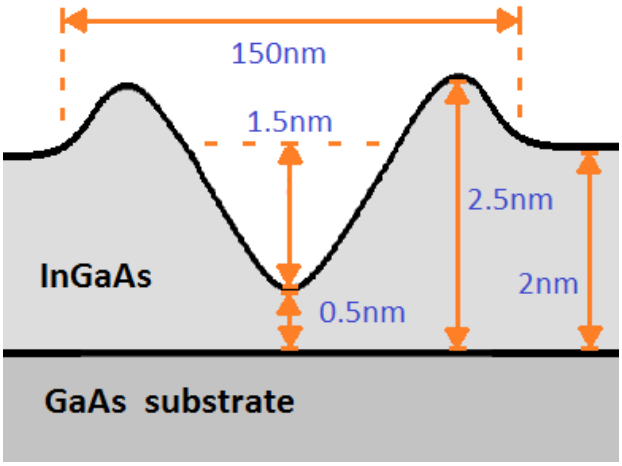

Figure 6.4: Schematic of the QR topography cross-section with typical dimensions marked. The rings were obtained by depositing 2nm of GaAs on QDs at the surface of a GaAs substrate.

QR center. Consistent with the observations made in Fig. 6.3, the superimposed topography and current cross-sections show that the lowest conductivity is measured in the central hole. The extent of low conductivity, however, is not limited to just the central (lowest) point of the QR hole. As we move radially outward from the center (and up the inner slope of the ring), the conductivity remains constant until a certain point where it starts to rise.

6.2.1 I-V measurements

To further investigate the conductivities of the central QR hole and the rim, I-V curves on both regions were measured (Fig. 6.6). In the measured I-V curves we observe that for all measured bias values the conductivity of the central hole is lower than that of the rim, consistent with Fig. 6.3. The QR on which the I-V curves were measured is shown in Figure 6.7. It was observed that the AFM scanner can experience drift between consecutive images (repeating a scan in the same position yields a slightly shifted image). Due to measurement noise it is not trivial distinguishing between individual QR rim and QR central hole I-Vs. To make sure that an I-V curve was taken at the desired position, the QR under investigation was repeatedly imaged after every few I-V curve measurements. We are therefore sure of the assignment of the curves to rim and hole.

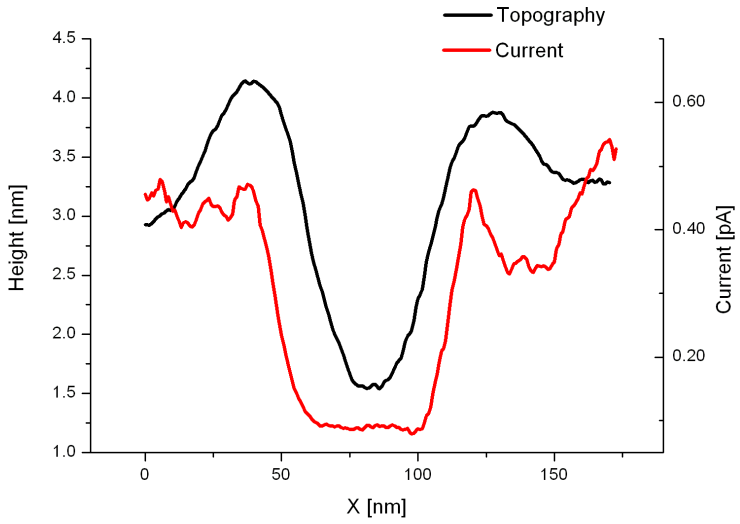

Figure 6.5: Topography and current cross-sections of a QR superimposed. The current cross-section is an average of 5 curves. The region of lowest conductivity is not limited to just the central point of the QR hole.

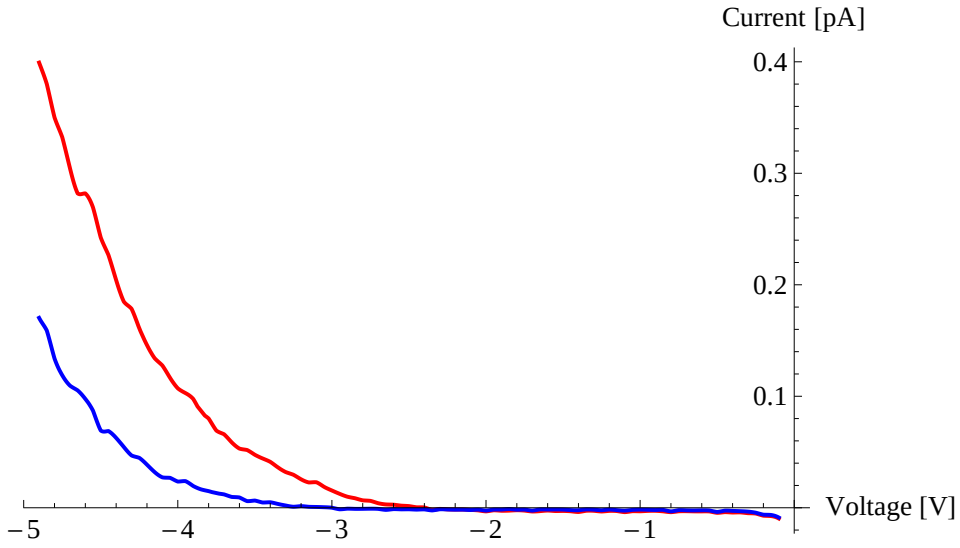

Figure 6.6: Measured I-V curves on QR rim (red) and central hole (blue), respectively. The red curve is an average of 109 individual I-V curves and the blue an average of 106 curves. The curves were acquired with a resolution of 0.05V and a sweep rate of $0.6V/s$, with a tip-sample force of around 45nN.

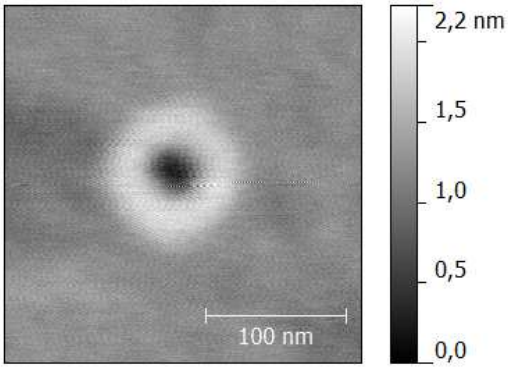

Figure 6.7: An AFM image of the quantum ring on which the I-V spectra were measured.

6.3 Discussion

C-AFM measurements on QDs yield results consistent with literature. Due to higher In content in the QDs, they exhibit a higher conductivity compared to the surrounding wetting layer. In QRs, the conductivites of the rim and WL are similar, and the central hole is the region of lowest conductivity. In order to understand this result, the composition of QRs needs to be examined.

6.3.1 QR composition

The available data on QR composition stems from investigations using x-ray photoemission electron microscopy (XPEEM) [42], cross-sectional scanning tunneling microscopy (XSTM) [43] and transmission electron microscopy (TEM) [44]. Here, we will describe the XPEEM measurements in more detail. For the topmost layer of the QR sample consisting of $In_xGa_{1-x}As$ with varying In content x, XPEEM measurements show that the In content is lowest in the capping layer ($x = 0.52$) and gradually rises towards the central QR hole, where it reaches its maximum ($x = 0.57$) (Fig. 6.8). However, for the interpretation of these numbers the photoemission process needs to be considered in more detail. It needs to be noted that with XPEEM the measured value of x is a weighted average of the compositions x_i of individual layers i at depth d_i (d is the monolayer thickness) according to the equation [45]

$$x = \frac{\sum_{i=0}^{\infty} x_i e^{-d_i/\lambda}}{\sum_{i=0}^{\infty} e^{-d_i/\lambda}}. \tag{6.1}$$

Given that the mean free path λ of the photoelectrons in this particular measurement is about 0.5nm [45] it is clear that the GaAs substrate layer (with zero In content) also contributes to the above value of x. Taking this into account we can extract the actual values of x for layers above the GaAs substrate using Eq. 6.1. For the central hole we get $x = 0.67$ and for the QR rim $x = 0.55$. These calculated values assume a uniform vertical composition profile for the layers above GaAs. This is an approximation since TEM and XSTM measurements have shown that In composition maxima occur at the interface to the GaAs substrate and at the surface (caused by accumulation of segregated In from the WL at the surface of the capping layer and by surface migration of In atoms that have been expelled from the QD during QR formation) [43, 44]. For the sake of simplicity, however, we will consider the relevant QR layers to be uniform, with the average indium compositions of $x = 0.67$ and $x = 0.55$ for the QR hole and rim, respectively.

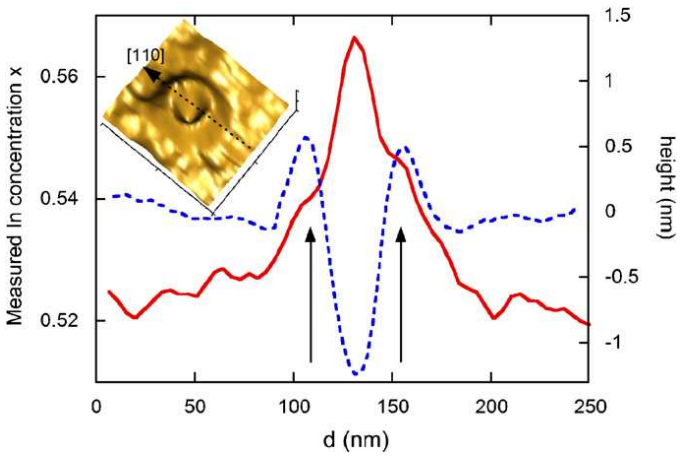

Figure 6.8: Solid line: XPEEM In composition profile of a QR, averaged over 10 scans. Dashed line: AFM height profile of a QR. Inset: AFM image of an InAs/GaAs QR [42].

6.3.2 C-AFM results

Since it has been previously established that InGaAs conductivity increases with increasing In content [40, 41], and since the central hole is the region of the QR

with the highest In content [42], one would expect in such a sample the central hole to be the region with highest conductivity. This is in clear contradiction with experimental results. However, it has to be considered that the sample was exposed to air before the conductivity measurements were performed, and so there is a surface oxide present (in contrast to the XPEEM measurements performed in UHV, where no such oxide is formed). Unlike in QDs, the influence of the oxide layer on the conductivity is expected to be more pronounced since the bottom of the QR central hole is at a height of only about 0.5nm above the GaAs substrate (see Fig. 6.4). By comparing the QR topography and current cross-sections (Fig. 6.5) the oxide thickness can be estimated. In Figure 6.5 we can observe that the region of lowest QR conductivity is not limited to just the lowest topographical point of the central hole. Under the assumptions that (i) the central regions of lowest conductivity correspond to a completely oxidized InGaAs layer, whereas regions of higher conductivity contain also an unoxidized InGaAs layer above the substate and that (ii) the thickness of the WL above the substrate is 2nm (assumed to equal the 2nm GaAs capping which leads to formation of QRs), one can estimate the oxide to be roughly 1nm thick (see Fig. 6.9 for further explanation). This value is in reasonable agreement with values reported for oxide layers on InAs [46, 47] and GaAs surfaces [48]. To confirm that a thin oxide layer on the QR samples can account for the unexpectedly lower conductivity of the central hole (given its high In content), numerical simulations of conductivities of different sample structures need to be performed. These are presented in the next chapter.

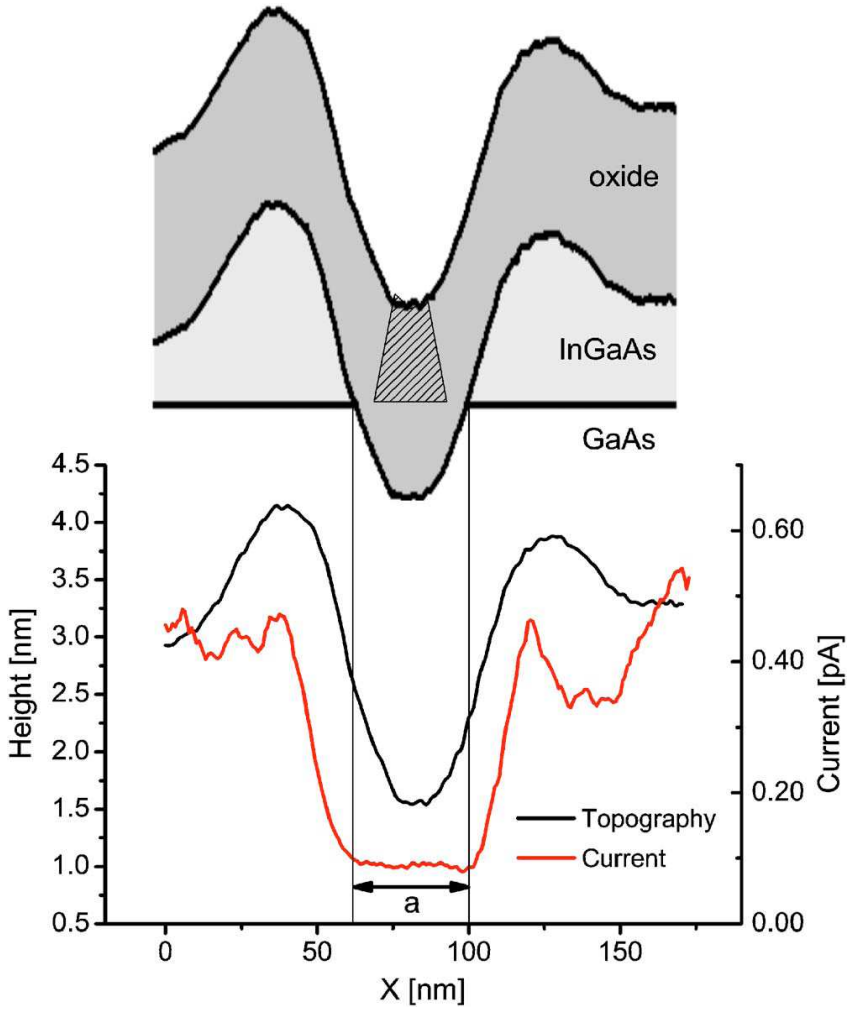

Figure 6.9: (Top) Composition schematic of a QR covered by a uniform oxide layer and (bottom) measured topography and current cross sections of a QR extracted from measurements as the one shown in Fig. 6.3. The region of lowest conductivity in the QR center extends from the central point radially outward and up the inner slope of the QR. The point on the slope where the conductivity starts increasing is about 1nm below the capping layer. From the capping layer thickness (∼2nm) we get an oxide thickness of about 1nm. The hatched area indicates the In-rich remainder of the original QD which has been measured by STM [43] and TEM [44].

Chapter 7

Current density modelling

C-AFM measurements of QRs, described in Chapter 4, yield surprising results given the material composition of different QR regions. The central hole is the region with the highest In content compared to the rim and the wetting layer (WL), and was thus expected to be the region with the highest conductivity. The opposite is observed: the conductvity of the central hole is lower than that of the rim and WL. However, due to the C-AFM samples being exposed to air, it is expected that a thin layer of surface oxide would have formed. In order to verify that the surface oxide can account for the observed conductivities of QR regions, measured I-V curves were compared to theoretically obtained curves for different sample strucutres.

The numerical procedure of obtaining I-V curves has been presented in chapter 3. For each sample structure the shape of the potential barrier was calculated with the 1D Poisson-Schrödinger simulator. From the barrier shape the transmission coefficient as a function of electron energy was obtained. Finally, the net current density through the barrier was calculated using the Tsu-Esaki formalism. The Tsu-Esaki formula assumes that the current flows from a metal to a semiconductor. To a first approximation, we treat the highly doped Si tip as a metallic electrode [49].

7.1 As-grown Quantum Rings

In order to obtain the conductivities of different QR regions in an oxide-free sample, numerical simulations of I-V curves on as-grown QRs were performed. The structures of the two QR sample regions (rim and center) input into the Poisson-Schrödinger simulator are shown in Table 7.1 and Fig. 7.1. These values are based on the results obtained in Chapter 4 (see Fig. 6.4).

QR hole	d [Å]	
InGaAs	5	$x = 0.67$
GaAs	1000	$N_d = 10^{18}/cm^3$

QR rim	d [Å]	
InGaAs	25	$x = 0.55$
GaAs	1000	$N_d = 10^{18}/cm^3$

Table 7.1: Sample structures used for numerical modelling of the energy bands. Top: unoxidized QR central hole. Bottom: unoxidized QR rim.

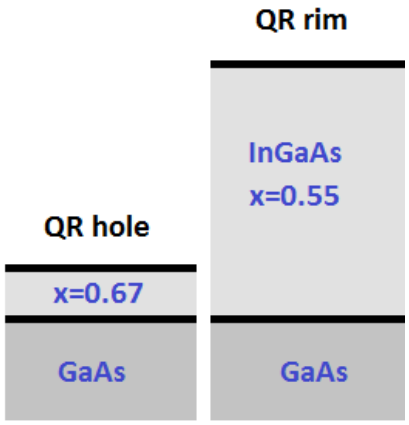

Figure 7.1: Schematic of the modelled sample structures.

The calculated shape of the potential barrier of a metal-semiconductor contact region is highly dependent on the height of the Schottky barrier. The Schottky barrier height depends on various factors such as work function of the AFM-tip metal coating, semiconductor band gap, type and concentration of dopants, interface quality and others. Additionally, the existance of surface states in semiconductors can result in Fermi level pinning which weakens the effect of the metal workfunction. In numerical simulations of the surface Schottky contact the *1D Poisson* software automatically assigns a Schottky barrier height of the surface material. The value used for the unoxidized rim region ($x = 0.55$) is 0.2eV which is reported in literature for $In_xGa_{1-x}As$ with $x = 0.53$ [50]. Taking into account that the Schottky barrier of InGaAs is suppressed completely for $x > 0.75$ [51], a barrier height of 0.1eV obtained by linear interpolation was used for the simulations of the ring center ($x = 0.67$). The results of the potential barrier calculations for zero and -5V bias are shown in Fig. 7.2. From the zero-bias result we can deduce that at low-bias values the GaAs/InGaAs conduction band discontinuity barrier is the limiting factor in tunneling. As the bias is increased (and the metal Fermi level shifted), the surface Schottky barrier becomes the dominant factor in electron transport (see inset of Fig. 7.2 - right). This is due to the fact that at room temperature, most of the electrons contributing to transport have an energy within few 10meV above the metal Fermi level and are thus affected mainly by the surface Schottky barrier.

Based on the calculated potential barriers I-V spectra, shown in Fig. 7.3, were calculated. Contrary to initial expectations, the central hole is not the region of

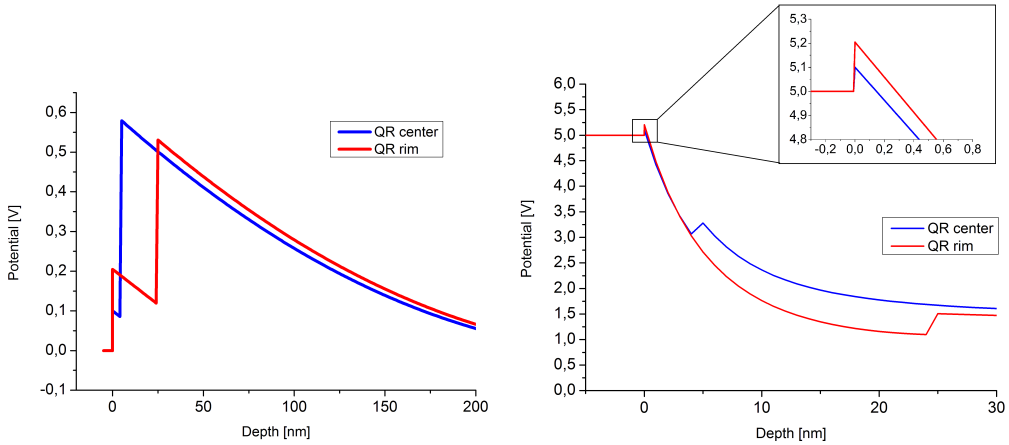

Figure 7.2: (left) QR rim and hole energy bands at zero surface bias. For low bias-values the GaAs/InGaAs conduction band discontinuity barrier is the limiting factor in transport. (right) QR rim and hole energy bands at -5V surface bias. (inset) At high negative bias the surface Schottky barrier height determines the tunneling current.

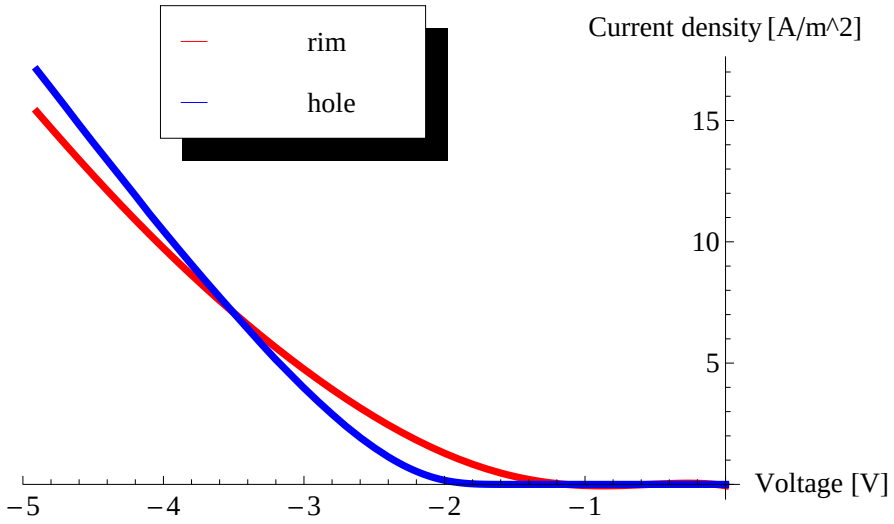

Figure 7.3: Numerical simulations of I-V curves for the rim and the central hole on unoxidized QRs. For low surface bias values the conductivity of the hole is lower compared to the rim. At higher surface bias the hole becomes more conductive.

highest conductivity for all applied surface bias values. The reason for this becomes clear if we examine the potential barriers at zero surface bias (Fig. 7.2 - left): the GaAs/InGaAs interface barrier height is lower below the rim than below the central hole which is a result of the GaAs/InGaAs interface being deeper under the surface in the case of the QR rim. As a result, the rim is more conductive compared to the central hole. As the negative bias is increased the surface InGaAs barrier gradually becomes dominant and since the In content is higher in the central region, the conductivity of this region will surpass the one of the rim (inset of Fig. 7.2 - right). Comparing the simulated I-V curves to the measured ones (Fig. 6.6) and taking into account that the region of lowest QR conductivity is not limited to just the central hole, it is clear that this model is not consistent with the experimental results. As a next step, a more complete model including a surface oxide layer is considered.

7.2 Quantum Rings with an oxidized surface

Numerical simulations of I-V spectra were repeated for samples where a surface oxide layer is considered. The material structures used in calculating the potential barriers, which are based on the results sketched in Fig.6.9, are shown in Table 7.2 and Fig. 7.4. The thickness of the oxide was taken to be 1nm (determined in Section 4.3.2). The oxide was simulated as a generic semiconductor with the bandgap as a parameter. Previous work on InGaAs oxides shows that oxide layers can be a mixture of different oxides (In, Ga, As oxides [52]) which range in bandgap values from 2.2eV for arsenic oxides [53], around 3.6eV for indium oxides [27, 54], and around 5eV for gallium oxides [55]. Here, we have chosen an oxide bandgap value of 2.8eV. The Schottky barrier for the oxide was taken to be one-half of the bandgap. It needs to be noted, however, that the results presented here do not crucially depend on the chosen values for these parameters, as varying the bandgap or the Schottky barrier height by $\pm 10\%$ yields the same qualitative results. The calculated barrier potentials (at zero surface bias) based on these input values are shown in Fig. 7.5.

Applying the transfer matrix method to the potential barrier yields, for the QR rim region at zero bias, the transmission coefficient dependency on incoming particle energy as shown in Fig. 7.6. Calculating the I-V spectra based on obtained energy band profiles yields the theoretical curves in Fig. 7.7 (dashed). We observe that the conductivity of the central hole now results to be lower than the one

QR hole	d [Å]	
oxide	10	$E_g = 2.8eV$
GaAs	1000	$N_d = 10^{18}/cm^3$

QR rim	d [Å]	
oxide	10	$E_g = 2.8eV$
InGaAs	15	$x = 0.55$
GaAs	1000	$N_d = 10^{18}/cm^3$

Table 7.2: Sample structures used for numerical modelling of the energy bands. Top: oxidized QR central hole. Bottom: oxidized QR rim.

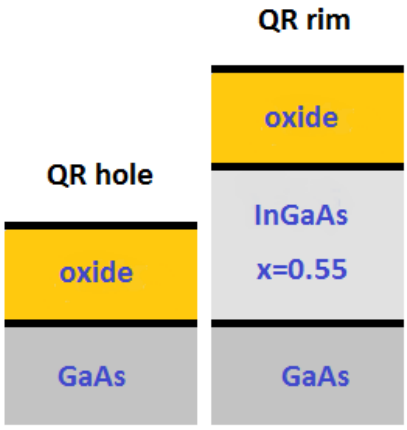

Figure 7.4: Schematic of the modelled sample structures.

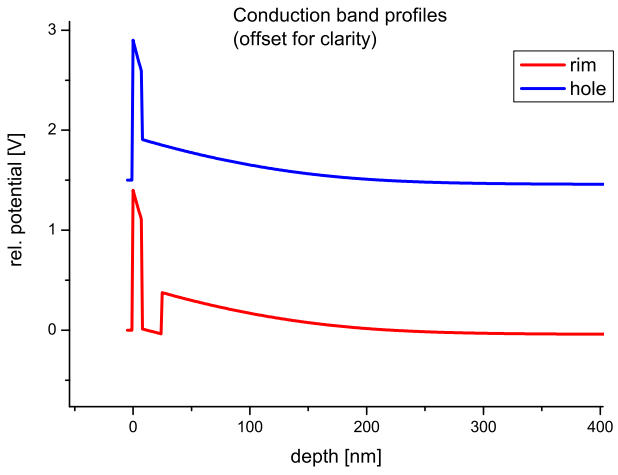

Figure 7.5: Band profiles of QR sample with the top layer oxidized - comparison between the rim and the central hole.

of the rim for the whole surface bias range investigated. Plotting the numerical results together with the measured I-V curves (Fig. 7.7) we find good qualitative agreement between theory and measurements. Surface oxide can thus explain the observed conductivities of different QR regions.

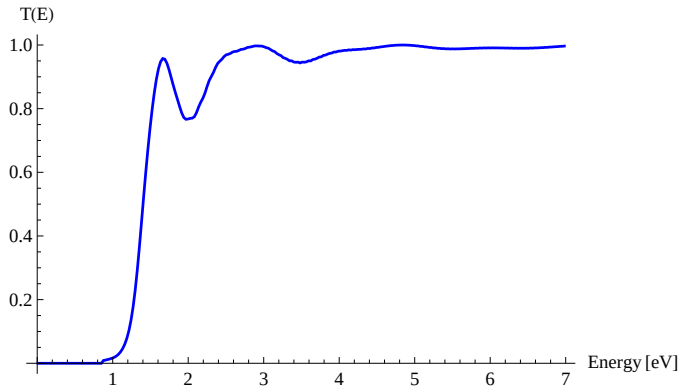

Figure 7.6: Transmission coefficient of the potential barrier of the QR rim with 1nm oxide at zero surface bias as a function of electron energy.

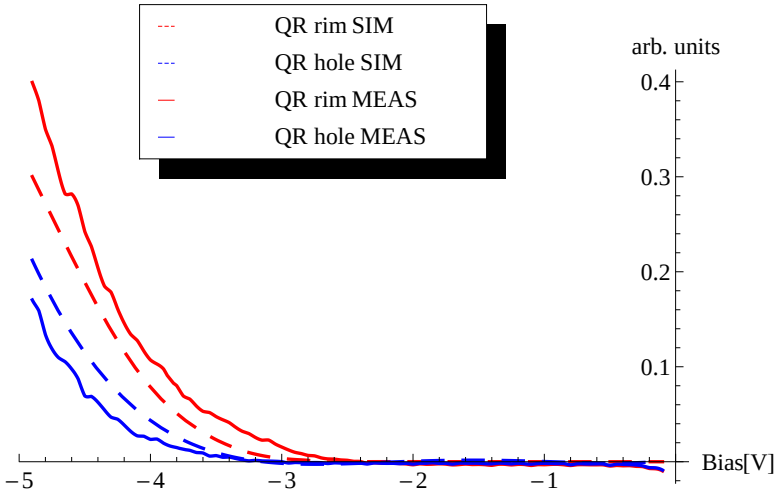

Figure 7.7: Comparison between the theoretical (dashed) and measured (solid) I-V curves. The good qualitative agreement of both sets of curves indicates that a surface oxide explains the observed conductivity.

Summary and conclusions

In this thesis, self-assembled InAs/GaAs quantum dot (QD) and quantum ring (QR) samples were studied using C-AFM. The measurements of QD samples yielded results consistent with literature: the QDs have a higher conductivity compared to the surrounding wetting layer due to the higher In content in the dots which lowers the Schottky barrier. On the other hand, two-dimensional current maps and local I-V spectra measured on QR samples show a lower conductivity of the central QR hole compared to the rim and capping layer for the whole bias range investigated. This result is surprising since XPEEM, XSTM and TEM measurements of the QR composition profile show that the central hole is the region with highest In content. Numerical simulations of I-V spectra show that apart from In content, the thickness of the individual QR regions is also a key factor in determining local conductivity. For the bias range investigated, simulations on as-grown samples show that for low bias values, a lower conductivity of the central hole is expected. For high bias, however, simulations show the central hole to be the region of highest conductivity. These results are incompatible with the experimental results, and therefore the model for the numerical simulations needed to be refined. Since the samples were exposed to air prior to C-AFM measurements, oxidation of the sample surface needs to be considered. Comparing the QR topography and conductivity cross-sections, we deduce an oxide height of about 1nm. Including the surface oxide layer into numerical simulations yields results which qualitatively agree with the measured conductivities and are consistent with the reported XPEEM results.

In order to verify the effect of surface oxidation on local conductivity, future investigations should focus on performing C-AFM measurements of QRs samples with an unoxidized surface. This would entail capping the grown samples with a protecting layer and transferring them to a C-AFM system in vacuum, where the capping would be removed prior to measuring.

Appendix A

Numerical routines for *Mathematica*

```
(*Transfer matrix calculus for quantum mechanical barrier problems*)

(*Constants*)

ev = 1.6 * 10^(-19);
hbar = 1.054 * 10^(-34);
mass = 9.11 * 10^(-31);

(*wave number in Å*)

k[En_, V_]:=Sqrt[2mass(En - V)ev]/hbar * 10^(-10);
(*Matrix defining continuity equations at an interface*)

T[x_, V_, En_]:={{Exp[I x u], Exp[-I x u]}, {I u Exp[I x u], -I u Exp[-I x u]}} /. u -> k[En, V];

(*Transfer matrix for single interface*)

TM[x_, V0_, V1_, En_]:=Inverse[T[x, V1, En]].T[x, V0, En];

(*Define reflection and transmission of a total transfer matrix*)

BLcoeff[t_]:= - t[[2, 1]]/t[[2, 2]];
ARcoeff[t_]:=t[[1, 1]] - t[[1, 2]]t[[2, 1]]/t[[2, 2]];

R[t_]:=Abs[BLcoeff[t]]^2;
T[t_]:=Abs[ARcoeff[t]]^2;
```

```
(*Define a procedure for partitioning a function into equally spaced step functions
between points a and b on the real line, with two semi-infinite steps outside the interval*)

(*Partition function*)

PartitionFunction[func_, a_, b_, n_, Vinit_:0, Vterm_:0]:=Module[{h, V},
h=(b-a)/n;
V = Table[func, {x, a, b - h, h}]; (*Collect n points f(a) to f(b-h)*)
V = AppendTo[V, Vterm]; (*Terminate potential*)
V = Insert[V, Vinit, 1]; (*Initial potential*)
Return[V]; ];

(*Define a procedure for calculating reflection and transmission for arbitrary functions
using n step function approximations*)

BarrierMatrix[En_, func_, a_, b_, n_, Vinit_:0, Vterm_:0]:=Module[{V, i, Temp, h},
h = (b - a)/n;
V = PartitionFunction[func, a, b, n, Vinit, Vterm];
Temp = IdentityMatrix[2];
For[i = 1, i < Length[V], i++,
Temp = TM[a + (i - 1)h, V[[i]], V[[i + 1]], En].Temp; ];
Return[Temp]; ];

BarrierTransmission[En_, func_, a_, b_, n_, Vinit_:0, Vterm_:0]:=Module[{Temp},
Temp = BarrierMatrix[En, func, a, b, n, Vinit, Vterm];
Return[{R[Temp], T[Temp] * k[En, Vterm]/k[En, Vinit]}]; ];

(*Define a function which returns a table of calculated transmissions for given energies*)

TMTable[func_, a_, b_, n_, Vinit_:0, Vterm_:0]:=Module[{pot, En, t, r, i, j, q, transmission},
pot = Max[Abs[PartitionFunction[func, a, b, n, Vinit, Vterm]]];
En = Table[x, {x, 0.01, 5pot, pot/20}];
t = En - En;
r = En - En;
For[i = 1, i ≤ Length[En], i++, q = BarrierTransmission[En[[i]], func, a, b, n, Vinit, Vterm];
t[[i]] = q[[2]]; ];
transmission = Table[{En[[j]], t[[j]]}, {j, 1, Length[En]}];
trans = Return[transmission];
];
```

```
(*Define the equation for calculating the current density through the barrier*)

Current[Efm_, Efs_, inter_]:=Module[{J, A, kbT},
kbT = 0.025;
J = NIntegrate[inter[x] * Log[(1 + Exp[(Efm - x)/kbT])/(1 + Exp[(Efs - x)/kbT])], {x, 0, ∞},
MaxRecursion → 200];
Return[J]; ];

(*Loop for importing data files and calculating the transmission for each imported barrier*)

CurrentDotWL = {};
For[i = 0, i ≤ 1,
For[j = 0, j ≤ 9,

(*Import barrier data from files "dotWL.ex.V-X.XX.out",
where X.XX is the surface voltage value*)

BandProfile = Import["dotWL.ex.V-" <> ToString[i] <> "."
<> ToString[j] <> "0.out", "TSV"];

(*Transform the data into a usable format*)

BandProfile = Delete[BandProfile, 1];
BandProfile = Flatten[BandProfile];

(*Extract depth and barrier height*)

depth = Take[BandProfile, {1, Length[BandProfile], 8}];
barr = Take[BandProfile, {2, Length[BandProfile], 8}];

(*Construct barrier data points*)

points = Table[{depth[[j]], barr[[j]]}, {j, 1, Length[barr]}];

(*Interpolate data points and calculate transmission*)

BarrierFunc = Interpolation[points];
TMTable[BarrierFunc[x], 0, 500, 800, 0, 0];
transmisivnost = Take[Flatten[trans], {2, 2 * Length[trans], 2}];
energies = Take[Flatten[trans], {1, 2 * Length[trans], 2}];

Do[Clear[m];
For[m = 2, m ≤ Length[transmisivnost]/2,
```

```
transmisivnost[[1]] = 10^ - 6;
If[transmisivnost[[m]] > 1||transmisivnost[[m]] < 0.01, transmisivnost[[m - 1]] = 10^ - 6];
m++;], {i, 5}];

(*Construct transmission data point*)

trans2 = Table[{energies[[j]], transmisivnost[[j]]}, {j, 1, Length[energies]}];

(*Interpolate data points*)

inter = Interpolation[trans2];

(*Calculate current density for given transmission*)

CurrentDotWL = Append[CurrentDotWL, Current[(10i + j)/10, -0.00001, inter]];

(*Plot transmission coefficient*)

Print[ListPlot[trans2, PlotRange → All, Joined → True]];
Print[10i + j];

j++];
i++];
```

Bibliography

[1] L. Kouwenhoven and C. Marcus, *Quantum dots*, Physics World, June 1998.

[2] L. Kouwenhoven, D. G. Austing, and S. Tarucha, *Few-electron quantum dots* Rep. Prog. Phys. **64**, 701-736 (2001).

[3] J. M. Elzerman, R. Hanson, L. H. Willems van Beveren, L. M. K. Vandersypen, and L. P. Kouwenhoven, Appl. Phys. Lett., **84** (2004) 4617.

[4] R. Blossey and A. Lorke, Phys. Rev. E **65** (2002) 021603.

[5] Figure taken from `http://www.ramehart.com/contactangle.htm`.

[6] R. J. Warburton, C. Schäflein, D. Haft, F. Bickel, A. Lorke, K. Karrai, J. M. García, W. Schoenfeld, and P. M. Petroff, Nature (London) **405** (2000) 926.

[7] Y. Aharonov and D. Bohm, Phys. Rev. **115** (1959) 485.

[8] A. Lorke, R. J. Luyken, A. O. Govorov, J. P. Kotthaus, J. M. Garcia, and P. M. Petroff, Phys. Rev. Lett. **84** (2000) 2223.

[9] N. A. J. M. Kleemans, I. M. A. Bominaar-Silkens, V. M. Fomin, V. N. Gladilin, D. Granados, A. G. Taboada, J. M. García, P. Offermans, U. Zeitler, P. C. M. Christianen, J. C. Maan, J. T. Devreese, and P. M. Koenraad, Phys. Rev. Lett **99**, (2007) 146808.

[10] A. Fuhrer, S. Lüscher, T. Ihn, T. Heinzel, K. Ensslin, W. Wegscheider, and M. Bichler, Nature **413**, (2001) 822.

[11] A. Z. Li, Z. M. Wang, J. Wu, and G. J. Salamo, Nano. Res. **3** (2010) 490.

[12] G. Biasiol, R. Magri, S. Heun, A. Locatelli, T. O. Mentes, and L. Sorba, J. Cryst. Growth **311** (2009) 1764.

[13] V. Baranwal, G. Biasiol, S. Heun, A. Locatelli, T. O. Mentes, M. N. Orti, and L. Sorba, Phys. Rev. B **80** (2009) 155328.

[14] T. Raz, D. Ritter, and G. Bahir, Appl. Phys. Lett. **82** (2003) 1706.

[15] J. Cui, Q. He, X. M. Jiang, Y. L. Fan, X. J. Yang, F. Xue, and Z. M. Jiang, Appl. Phys. Lett. **83** (2003) 2907.

[16] A. Lorke, R. J. Luyken, J. M. Garcia, and P. M. Petroff, Jpn. J. Appl. Phys. **40** (2001) 1857.

[17] A. Lorke, R. Blossey, J. M. Garcia, M. Bichler, and G. Abstreiter, Mater. Sci. Eng. B **88** (2002) 225.

[18] M. A. Herman and H. Sitter, *Molecular Beam Epitaxy*, Springer-Verlag, Berlin (1996).

[19] C. T. Foxon and B. A. Joyce, Surf. Sci. **64** (1977) 293.

[20] D. Sarid, *Scanning Force Microscopy*, Oxford University press, Oxford (1994).

[21] M. Dreyer and R. Wiesendanger, Appl. Phys. **A 61** (1995) 357.

[22] P. De Wolf, M. Geva, T. Hantschel, W. Vandervorst, and R. B. Blysma, Appl. Phys. Lett. **73** (1998) 2155.

[23] M. Nonnemacher, M. P. O'Boyle, and H. K. Wickramasinghe, Appl. Phys. Lett. **58** (1991) 2921.

[24] S. Morita and Y. Sugawara, Thin Solid Films **393** (2001) 310.

[25] P. Avouris, T. Hertel, and R. Martel, Appl. Phys. Lett. **71** (1997) 285.

[26] S. Kremmer, H. Wurmbauer, C. Teichert, G. Tallarida, S. Spiga, C. Wiemer, and M. Fanciulli, J. Appl. Phys. **97** (2005) 074315.

[27] K. Smaali, M. Troyon, A. El Hdiy, M. Molinari, G. Saint-Girons, and G. Patriarche, Appl. Phys. Lett. **89** (2006) 112115.

[28] C. Teichert and I. Beinik, Conductive Atomic-Force Microscopy Investigation of Nanostructures in Microelectronics. In B. Bhushan (Ed.), *Scanning Probe Microscopy in Nanoscience and Nanotechnology*, Vol. 2 (pp. 691-721), Springer Berlin 2011.

[29] X. Blasco, J. Petry, M. Nafria, X. Aymerich, O. Richard, and W. Vandervorst, Microelectron. Eng. **72** (2004) 191.

[30] K. Bouzehouane, S. Fusil, M. Bibes, J. Carrey, T. Blon, M. Le Du, P. Seneor, V. Cros, and L. Vila, Nano Lett. **3** (2003) 1599.

[31] L.S.C. Pingree, O.G. Reid, and D.S. Ginger, Adv. Mater. **21** (2009) 19.

[32] M. Ishikawa, M. Yoshimura, and K. Ueda, Jpn. J. Appl. Phys. **41** (2001) 4908.

[33] R. Tsu and L. Esaki, Appl. Phys. Lett. **22** (1973) 562.

[34] M. Furno, F. Bonani, and G. Ghione, Solid-State Electron. **51** (2007) 466.

[35] The *1D Poisson* solver is available at `http://www.nd.edu/~gsnider`.

[36] I-H. Tan, G. L. Snider, L. D. Chang, and E. L. Hu, J. Appl. Phys. **68** (1990) 4071.

[37] W. W. Lui and M. Fukuma, J. Appl. Phys. **60** (1986) 1555.

[38] The routines are based on *Transfer matrix calculus for quantum mechanical barrier problems* by N. Dougherty, obtained via private communication.

[39] I. Tanaka, I. Kamiya, H. Sakaki, N. Qureshi, S. J. Allen, and P. M. Petroff, Appl. Phys. Lett. **74** (1999) 844.

[40] Y. Okada, M. Miyagi, K. Akahane, Y. Iuchi, and M. Kawabe, J. of Appl. Phys. **90** (2001) 192.

[41] H. Yamamoto, T. Takahashi, and I. Kamiya, Appl. Phys. Lett. **77** (2000) 1994.

[42] G. Biasiol, V. Baranwal, S. Heun, M. Prasciolu, M. Tormen, A. Locatelli, T. O. Mentes, M. A. Niño, and L. Sorba, J. Cryst. Growth **311** (2009) 1764.

[43] P. Offermans, P. M. Koenraad, J. H. Wolter, D. Granados, J. M. Garcia, V. M. Fomin, V. N. Gladilin, and J. T. Devreese, Appl. Phys. Lett. **87** (2005) 131902.

[44] D. Granados, J. M. Garcia, T. Ben, and S. I. Molina, Appl. Phys. Lett. **86** (2005) 071918

[45] G. Biasiol, S. Heun, and L. Sorba, J. Nanoelectron. Optoelectron. **6** (2010) 20.

[46] D. Y. Petrovykh, M. J. Yang, and L. J. Whitman, Surf. Sci. **523** (2003) 231.

[47] A. Zolotaryov, A. Bolz, A. Schramm, W. Hansen, and R. L. Johnson, Phys. Stat. Sol. (a) **204** (2007) 2662.

[48] A. F. Pun, X. Wang, S. M. Durbin, and J. P. Zheng, Thin Solid Films **515** (2007) 4419.

[49] S. Pal, M. K. Sanyal, N. S. John, and G. U. Kulkarni, Phys. Rev. B **71** (2005) 121404(R).

[50] H. Tamura, A. Yoshida, S. Muto, and S. Hasuo, Jpn. J. Appl. Phys. **26** (1987) L7.

[51] D. Uhlisch, M. Y. Kupriyanov, A. A. Golubov, J. Appenzeller, T. Klocke, K. Neurohr, A. V. Ustinov, and A. I. Braginski, Physica B **225** (1996) 197.

[52] G. Hollinger, R. Skheyta-Kabbani, and M. Gendry, Phys. Rev. B **49** (1994) 11159

[53] C. M. Finnie and P. W. Bohn, Appl. Phys. Lett. **74** (1999) 1096

[54] A. Walsh, J. L. F. Da Silva, S-H. Wei, C. Körber, A. Klein, L. F. J. Piper, Alex DeMasi, K. E. Smith, G. Panaccione, P. Torelli, D. J. Payne, A. Bourlange, and R. G. Egdell, Phys. Rev. Lett **100** (2008) 167402.

[55] Z. Ji, J. Du, J. Fan, and W. Wang, Opt. Mat. **28** (2006) 415